aerospace

MDPI

Article

Smart Ground Support Equipment—The Design and Demonstration of Robotic Ground Support Equipment for Small Spacecraft Integration and Verification

Sebastian Kottmeier [1,*], Philipp Wittje [1], Sabine Klinkner [2], Olaf Essmann [1], Birgit Suhr [1], Jan-Luca Kirchler [1] and Tra-Mi Ho [1,*]

[1] German Aerospace Center (DLR), Institute of Space Systems, Robert-Hooke-Straße 7, 28359 Bremen, Germany; philipp.wittje@protonmail.com (P.W.); olaf.essmann@dlr.de (O.E.); birgit.suhr@dlr.de (B.S.)

[2] Institute of Space Systems, University of Stuttgart, Pfaffenwaldring 29, 70569 Stuttgart, Germany; klinkner@irs.uni-stuttgart.de

* Correspondence: sebastian.kottmeier@dlr.de (S.K.); tra-mi.ho@dlr.de (T.-M.H.); Tel.: +49-(0)-421-24420-1253 (S.K.); +49-(0)-421-24420-1171 (T.-M.H.)

Abstract: In order to reduce the costs of integration and verification processes and to optimize the assembly, integration and verification (AIV) flow in the prototype development of small- and medium-sized spacecrafts, an industrial six-axis robot was used as a universal mechanical ground support equipment instead of a tailored prototype specific ground support equipment (GSE). In particular, a robotic platform offers the possibility of embedding verification steps such as mass property determination into the integration process while offering a wider range of ergonomic adaption due to the enhanced number of degrees of freedom compared to a classical static Mechanical GSE (MGSE). This reduces development costs for projects and enhances the flexibility and ergonomics of primarily mechanical AIV operations. In this paper, the robotic MGSE system is described, the operational prospects for in-line verification are elaborated and an example is given showing the possibilities and challenges of its operational use as well as its in-line mass determination capabilities. For this purpose, a method has been developed that allows for the precise measurement of the spacecraft mass using the robot's existing technology without the need for additional hardware. Subsequent work will extend this to determine the center of gravity and the moments of inertia of the payload on the robotic MGSE.

Keywords: spacecraft AIV; smart ground support equipment; robotic AIV; in-line mass determination

Citation: Kottmeier, S.; Wittje, P.; Klinkner, S.; Essmann, O.; Suhr, B.; Kirchler, J.-L.; Ho, T.-M. Smart Ground Support Equipment—The Design and Demonstration of Robotic Ground Support Equipment for Small Spacecraft Integration and Verification. *Aerospace* **2024**, *11*, 279. https://doi.org/10.3390/aerospace11040279

Academic Editor: Norman M. Wereley

Received: 23 January 2024
Revised: 15 March 2024
Accepted: 28 March 2024
Published: 31 March 2024

1. Introduction

After the successful launch of the compact satellite mission Eu:CROPIS (Euglena Combined Regenerative Organic-Food Production in Space) at the German Aerospace Center (DLR) in December 2018, the involved spacecraft AIV team started a deep-rooted analysis of the lessons learned during the integration and verification campaigns of the Eu:CROPIS spacecraft [1]. The process aimed to identify fields in which the AIV flow of small- and medium-scale prototype spacecrafts could be streamlined in order to reduce the overall non-value-adding activities by means of improved team organization, documentation flow, tools and infrastructure. In this context, two key aspects are identified:

A. The recurring need to design, produce, verify and operate spacecraft mechanical ground support equipment (MGSE) fitted to the respective prototype spacecraft and project.
B. The recurring need to attach and detach the spacecraft to and from the MGSE for integration, logistics and testing.

To cover the given lessons learned, the design and usage philosophies of spacecraft MGSE have been further analyzed in order to propose more advanced ways of handling spacecraft for future projects. In general, spacecraft MGSE has to comply with the following requirements:

- Accommodate a space system in integration;
- Position and hold the system in integration in a defined spatial position;
- Provide at least two rotational degrees of freedom;
- Support integration by means of ergonomics;
- Support transport activities (floor transport, lifting operations).

A standard approach in MGSE designs, as seen in the commercial spacecraft sector, is a trolley setup with a toggle–lever platform and an additional rotational axis perpendicular to the spacecraft interface plane; see Figure 1. This design allows for robust and safe positioning of the systems but has considerable limitations in terms of accessibility during integration, so gantries or comparable devices must be used.

Figure 1. Basic MGSE design [2].

For small- and medium-size scientific spacecraft, such as the compact satellite Eu:CROPIS, the MGSE design is driven not only by safety and handling aspects but also by the specific demands of the actual spacecraft design. This requires a departure from a standard approach towards individual solutions that are developed, manufactured and tested in parallel to the space system. This binds additional engineering resources and increases project costs for manufacturing, certification and maintenance. Furthermore, the need to perform spanning operations for all activities during the verification phase, such as lifting and test facility setup, increases the cost and risk of assembly, integration and verification.

It is therefore proposed to replace the classical MGSE with a standard, high-performance, six-axis industrial robot with a load capacity between 300 and 600 kg to reduce dedicated MGSE development and to maximize the cross-project usability while opening a wider range of use cases coming with additional degrees of freedom [3].

This paper aims to describe the system setup of such a robotic ground support equipment (RGSE) to provide an overview of the system's capabilities in terms of hardware handling and in-line verification, including the results of a feasibility study performed for an in-line mass determination algorithm.

2. Materials and Methods

2.1. Robotic Smart GSE Design Rationale

An industrial robot equipped with a universal interface at its hand mount avoids the need for major adaptations for different spacecraft prototypes to be integrated, see Figure 2. Due to the mechanics of the robot, an almost free positioning of the system during integration in all six degrees of freedom is possible, allowing better ergonomics for the operators without the need for additional clamping and repositioning. Furthermore, the automation capabilities of an industrial robotic system allow for the automation of several aspects of the integration and verification process. In combination with a self-driving platform trolley, the system can be freely moved in the integration facility, reducing the need for additional external logistics equipment.

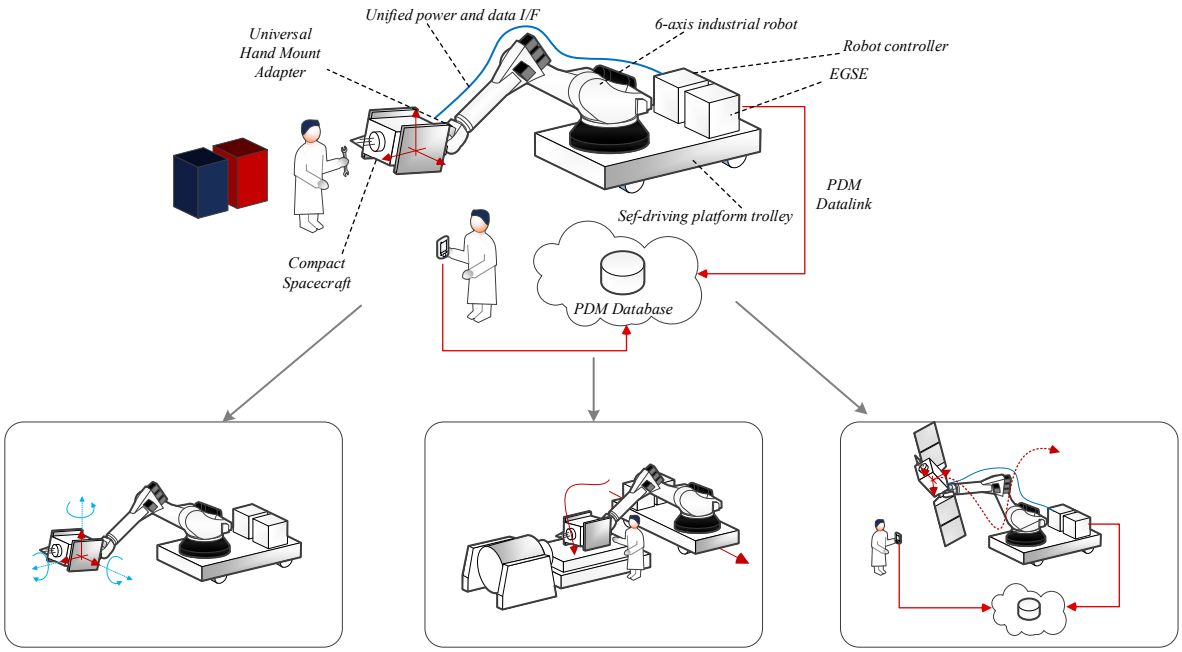

Figure 2. Principal setup of a robotic ground support equipment for small spacecraft and possible use cases: integration logistics, in-line mass property determination, logistics support and AOCS open-loop testing as figures.

The autonomous generation of kinematic and position-related data and the ability to perform in-line verification can be used in close collaboration with a Product Data Management (PDM) solution, a database system that stores and manages any hardware-related engineering information. A suitable PDM solution for cooperation with the Smart GSE is currently under development at DLR in the COOPERANTS project of the GAIA-X initiative [4].

Such a robotic system is helpful for a variety of use cases. The most important ones are briefly described below.

2.1.1. Optimizing Ergonomics during Operation in Close Human–Robot Collaboration

The operational envelope of the robot allows the payload to rotate freely in space and to adapt the Cartesian position perfectly to the needs of the respective operator. This improves work speed and quality and offers relief to operators, thus preserving health and preventing work-related accidents. In combination with a PDM database, automatic positioning can be realized based on both the operator's physique and the integration procedures (Figure 3).

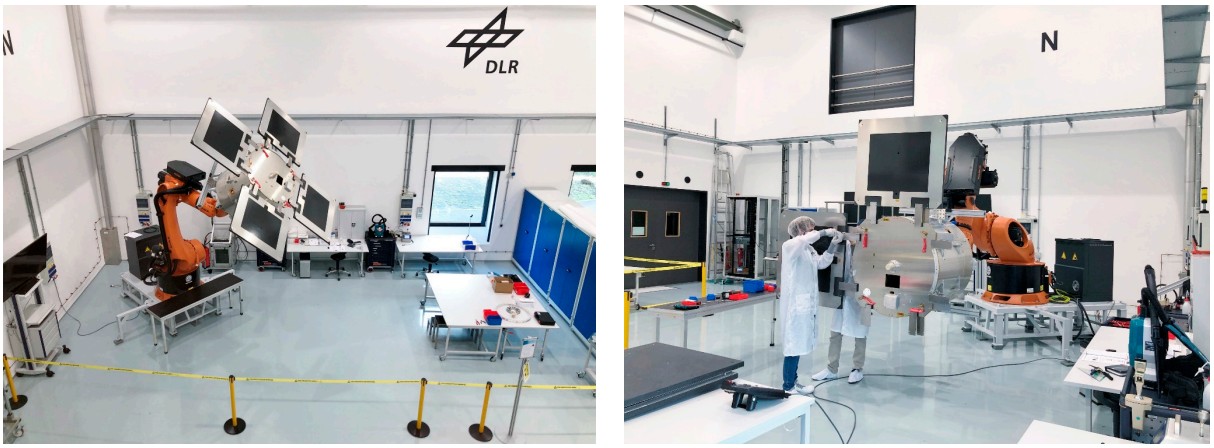

Figure 3. Robotic ground support equipment holding the compact satellite Eu:CROPIS at the DLR integration facility in Bremen (**left**); demonstration of RGSE-assisted integration of solar arrays (**right**).

2.1.2. In-Line Determination of Mass Properties

In addition to the new possibilities for on-site handling that the robot offers due to the freedom of movement of the prototype in space, the robot can also be used to carry out some of the mandatory verification tests, which previously required considerable logistical and financial expenditure. One of the many possibilities offered by the robot in this context is the determination of the mass properties by means of the technology provided by the robot itself. This technology is already available off the shelf for standard industrial applications, but a review of the offered software solutions showed that a transfer to space applications is not easily possible:

- The overall accuracy of the reviewed off-the-shelf solution is too low for the ECSS requirements [5].
- The MCI determination for tools uses very high speeds to apply necessary accelerations. This is not feasible with space payloads in terms of safety and operational constraints.
- The suggested system implementation involves a non-standard operation of the robot, placing a large payload outside the CoG envelope of the robot system, which is only possible when the angular rates and thus the axis torques are kept low.

Due to these reasons, we tried to implement a simple yet space-sufficient solution for in-line MCI determination. The intended algorithm consists of the mass determination, the center of gravity determination and the determination of the moments of inertia (MCI), all performed as individual, independent measurements. With an attached PDM system, the measured parameters can be directly fed into the engineering database.

2.1.3. In-Line 3D Surface Measurements

Since the robot is able to re-orientate to any given position in its envelope within a well-defined accuracy, it is possible to use the robot for three-dimensional surface analysis. To do so, a well-defined, rigid coordinate point is placed within the operating envelope. The position of the coordinate points is known with respect to the robot base coordinate frame R. Kinematics can be used to position the surface features of the test specimen on the coordinate point and to measure both Euler angles and Cartesian positions. This setup can be seen as an inverse coordinate measurement technique. The system can also help to automatize the usage of surface laser-line scanning devices.

2.1.4. Open- and Closed-Loop Testing of Attitude and Orbit Control Systems

The operational envelope of the robot kinematics allows for the playback of pre-defined attitude disturbances. A spacecraft attached to the robot hand mount can then, within a hot-fire plugs-out test, react to the induced disturbances by counter-actuating its attitude control system. This case of open-loop simulation allows for a functional check of

the attitude control system elements. When a feedback loop is integrated into the system, the robot can counteract the AOCS (Attitude and Orbit Control Systems) forces via a simulation interface. This would allow for closed-loop testing of the attitude control system during a plugs-out test on the ground, thus providing information on the quality of the control algorithms.

This work is currently in a very early state. So far, we conducted small studies on sub-scale systems to evaluate the possibilities of AOCS functional tests and the reduction in disturbance effects such as friction, specifically for the verification of this particular subsystem. A future publication will address this topic.

2.1.5. Automated Optical Alignment

Since geometrical repeatability, as explained above, is a key feature of an industrial robot, it can be used for the alignment of coordinate frames for inertial measurement units or optical sensors. It is possible to set up a known optical measurement coordinate frame aligned to the robot base coordinate frame in a way that an optical alignment device, such as an alignment cube, can be repeatedly placed in the integration facility, providing knowledge of the absolute position and Euler angles. This drastically reduces the complexity of the optical measurement setup and speeds up the actual alignment process. With the connection to a PDM database, the absolute position and rotation of the optical alignment device could be directly derived from CAD data and transferred to the robot controller in the form of a command script.

2.1.6. Optimized In-House Logistics

During the integration of prototypes, certain verification steps are planned at different milestones in order to verify the requirements, document the progress and verify the correctness of the assembly steps carried out. Depending on the verification needs, the spacecraft has to be removed from the MGSE and transported to the respective test facilities. These test facilities are not always available on-site, so the spacecraft may have to be transported longer distances by road or other means. This procedure accumulates many spanning- and consecutive-floor transport steps, which, in consequence, generate accompanying PA processes (Figure 4).

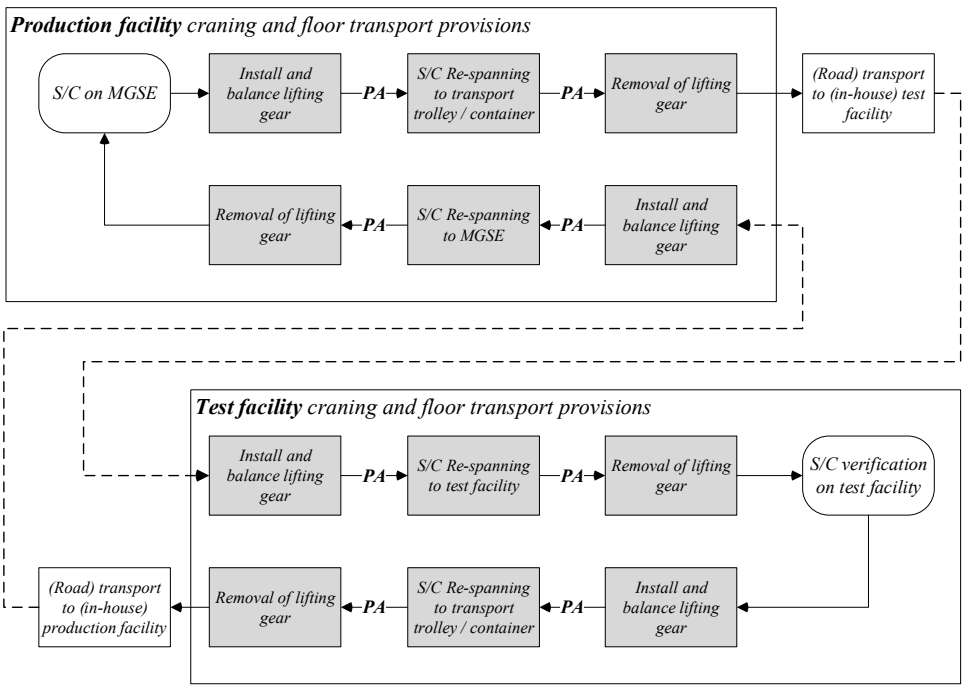

Figure 4. Regular approach of spacecraft in-house and inter-facility logistics.

A mobilized RGSE would bring a new perspective to the in-house logistics subset of the general transportation problem. The described system is able to cover a lot of the in-house logistics processes, such as craning. In the same approach, it is superseding some of the necessary processes, since many verifications could be covered by in-line testing without the necessity of an external test facility. As can be seen in Figure 5, the most prominent effect is expected in the field of on-site logistics and testing. If internal logistics processes can be performed without the need for re-spanning operations, the overall operational and product assurance effort would be drastically reduced.

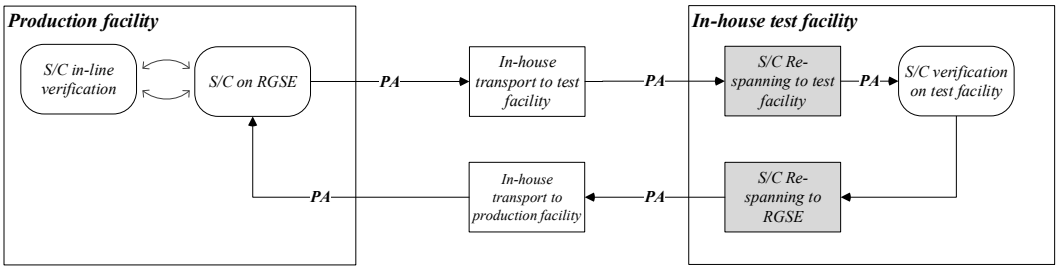

Figure 5. RGSE enabled impact on spacecraft in-house logistics.

In the field of inter-facility logistics, the expected impact on operational optimization concentrates on the on-site activities during loading operations; thus, the effect is limited to only a small proportion of the overall logistics effort (Figure 6).

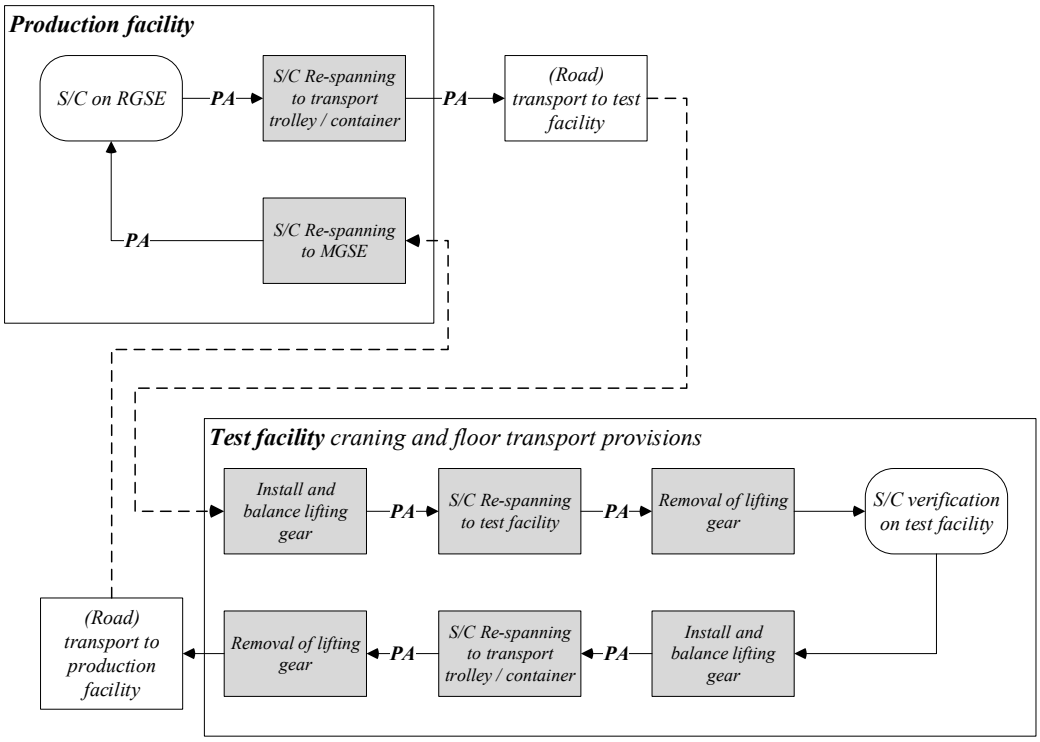

Figure 6. RGSE enabled impact on spacecraft inter-facility logistics.

To determine the feasibility of the features described in this section, a robotic platform was specified and designed. In several consecutive steps, the different suggested methods will be set up and examined, starting with the mass property determination, which is deemed to be the most basic yet most powerful in-line verification approach. The ergonomics of the setup were extensively tested during the structural- and flight-model integration campaigns of the Martian Moon Exploration Mission (MMX) rover [6] as well

as the structural model campaign of the Reusability Flight Experiment (ReFEx) [7]. The derivation of the MCI algorithm is described in the following sections.

By now, the given hypothesis of an overall productivity and safety gain, as described in Figures 4–6, is based on the total countable actions per process, assuming that a higher number of actions will increase the chance of failure, thus increasing the overall risk. Currently, a broad study to evaluate the actual process key performance indicators, such as the station time and production efficiency factor, is performed comparing a standard GSE approach with a fully integrated smart GSE approach. The study is based on the compact satellite Eu:CROPIS as an example of a "classical" spacecraft production process and the ongoing projects MMX, ReFEx and CALLISTO, and shall give an insight into the cost structure and return of investment (RoI) of the Smart GSE approach.

The results will be presented in future works.

2.2. System Description

The robotic platform used to examine the feasibility of a smart GSE is shown in detail in Figure 7. The robot used is a KUKA KR500 R2830 built in 2015 with a KR-C4 controller (KRC4 SC2 X11 X51 X66 IO). Both the robot and controller are mounted to a steel frame with a height of 600 mm to enhance the range above ground. The robot has six axes, labeled *A1* to *A6*, which are moved by servo motors with incremental encoders and an attached gearbox (Figure 8). The repeatability accuracy, i.e., the accuracy with which the robot can approach a defined position with defined Euler angles, is defined in ISO 9283 and given with ± 0.08 mm [8]. Since the precise motor position plays an important role in the accuracy of the mass determination method developed here, it can be argued that the smallest possible deviation in repeatability leads to better accuracy in weight measurement. The robotic platform weighs approximately 3000 kg in total, which severely limits the options to apply any mobility-enhancing systems. The mobilization of the RGSE is foreseen for a later point in the ongoing development.

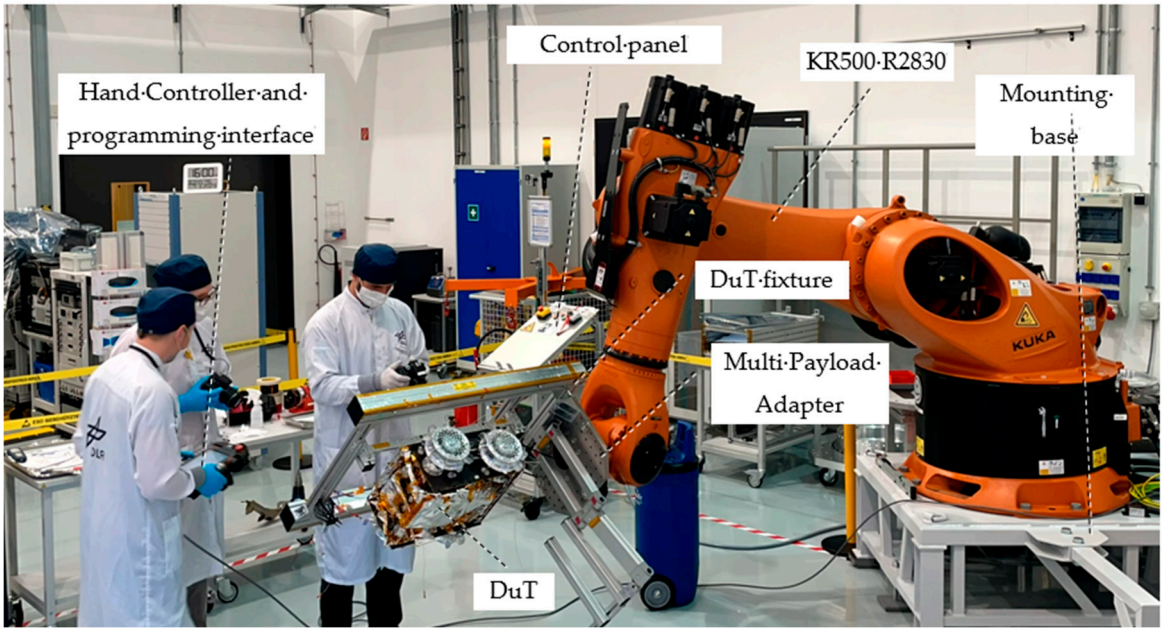

Figure 7. RGSE feasibility for integration assistance demonstrated in the frame of the MMX Rover *Idefix* at DLR Bremen.

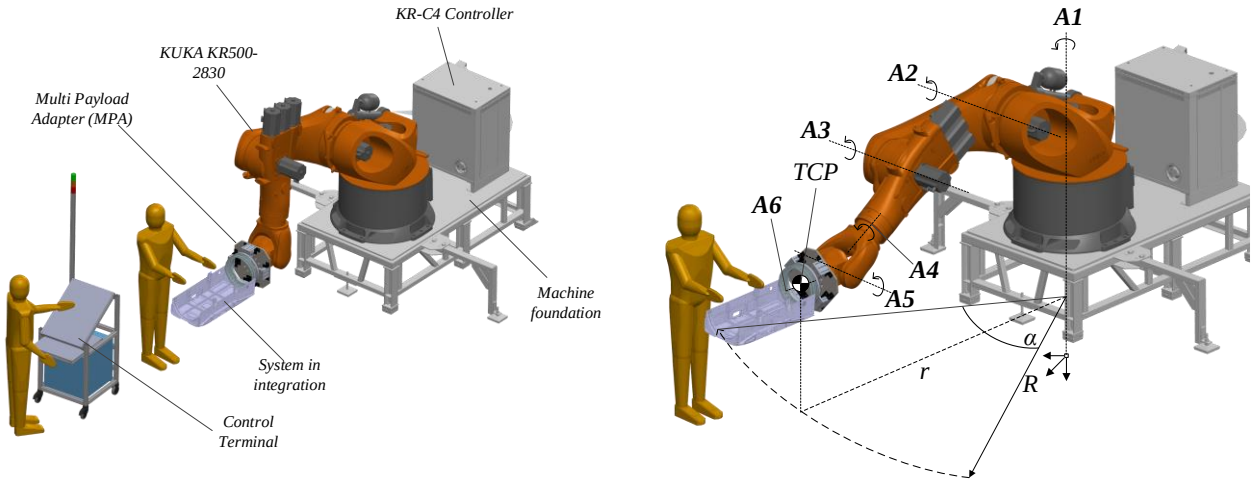

Figure 8. Robotic platform design (**left**) and robot axis definition (**right**).

The system is locked programmatically in a software-defined envelope of ±45° around axis *A1* to prevent any tip-over events and to limit the size of the hazard area when the robot is operated in automatic modes. The maximum achievable, stable horizontal range r in this setup is 2800 mm. For human–robot interaction, the robotic platform is operated in test mode T1 with the hand controller interface. In this mode, the maximum Cartesian speed of each element of the kinematic chain is limited to 200 mm/s with a mandatory Deadman control, thus minimizing the risk of injuries. For all envisaged verification tests, usage of the T1 mode is preferred. If it should be necessary to deviate to a fully automatic mode for an automated test sequence, the hazard area has to be cleared and cordoned off. A keylock in the control panel is used as a second security feature to prevent the accidental activation of automatic motions.

For the attachment of payloads to the robot hand mount flange, a multi-payload adapter (MPA) was designed. This adapter consists of a 20 mm thick stainless-steel plate with external dimensions of 440 × 440 mm. A centered 40 mm M8 hole pattern is used to mount the external payloads. A central cut-out with a diameter of ø120 mm allows a direct line-of-sight to the hand mount Tool Center Point (TCP).

For all activities described in this paper, a set of stackable calibration weights with the same outer dimensions as the MPA was used to simulate an actual payload.

In order to be able to use an industrial robot for verification purposes, externally mounted force–torque sensors are commonly sold as standard equipment. These sensors are mounted on the hand flange, providing an interface to the actual payload and enabling the external determination of mass properties with high precision. However, in order to keep the acquisition costs low, it has been decided not to use such a system and instead to develop a low-cost, low-maintenance method using the technology already available on the robotic platform. This method uses reference measurements with defined weights, motor current-based axis torques, and the known mechanical properties of the robot. The method is so generic that it is theoretically transferable to any other multi-axis robot.

For ergonomic purposes, a modular and flexible workspace concept is a key element.

The surrounding workspace must be able to quickly adapt to the RGSE setup. The design of this concept is an ongoing development that has been tested and demonstrated for the projects MMX, ReFEx and CALLISTO (Figures 9 and 10) and will be subject to future publications.

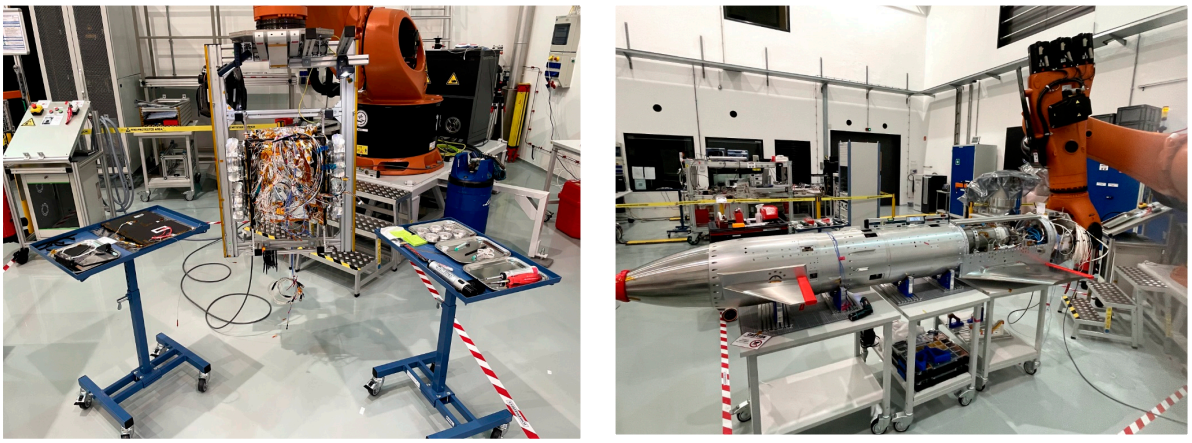

Figure 9. RGSE modular workspace concepts: MMX rover chassis harnessing (**left**) and mating of the ReFEx fuselage segments (**right**).

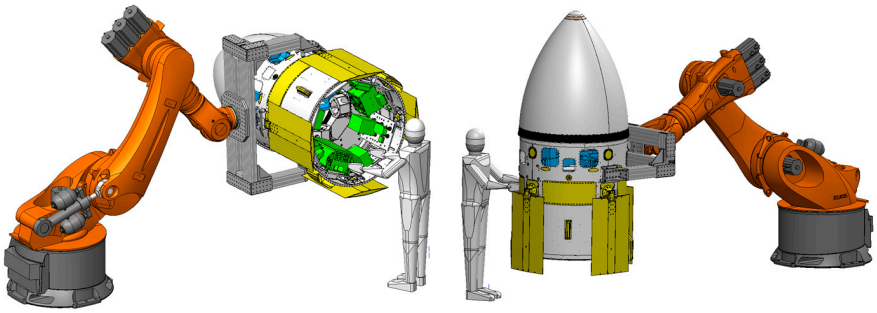

Figure 10. Concept of operation for the CALLISTO top block structural model campaign [9].

2.3. Mass Property Determination

2.3.1. Theoretical Consideration

The mass properties of spacecraft are composed of the object mass, the position of the center of gravity in three axes relative to a base coordinate frame and the inertia matrix relative to the CoG coordinate frame. A simplified MCI system is given in Figure 11.

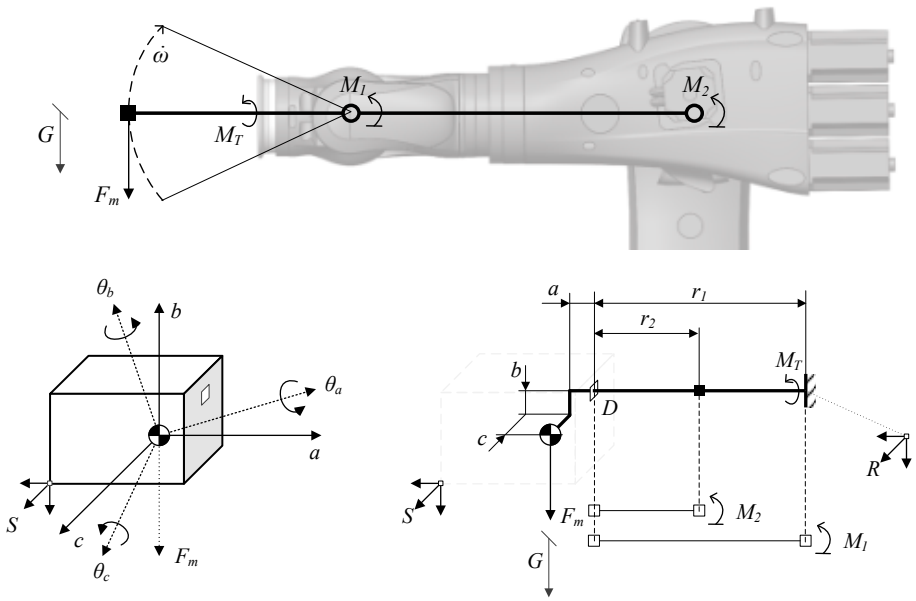

Figure 11. Principal mass property system of a body of inhomogeneous density, reduced mechanical system, mass and CoG determination.

A 6-DoF robotic ground support equipment is capable of determining all three parameters without removing the device under test (DuT) from the hand mount. The mentioned mass properties for a body of unknown CoG position can be consecutively measured using three output torques around the robot axes for defined rotations and movements since all tests use the same baseline measurement principle.

Figure 10 shows the basic physical principles for the MCI determination algorithm. For mass determination of a body of unknown CoG, a lever system with two known lengths, r_1 and r_2, is used to measure the torque at two measurement points: M_1 and M_2. The interface position D, as well as the coordinate transformation from robot to body $R \rightarrow S$, is known.

For the derivation, the lever system is assumed to be massless. The resulting torques are defined by the lever system lengths and the yet unknown CoG lever a:

$$M_1 = (r_1 + a)F_m \tag{1}$$

$$M_2 = (r_2 + a)F_m \tag{2}$$

Introducing DuT mass and gravitational acceleration to the equation system leads to the following:

$$M_1 - M_2 = m_{DuT}\, g\, ((r_1 + a) - (r_2 + a)) \tag{3}$$

$$m_{DuT} = \frac{M_1 - M_2}{g\,(r_1 - r_2)} \tag{4}$$

With the known body mass, the CoG coordinate a can be determined in the originating R frame using the linear moment M_2:

$$a = \frac{M_{2,0^\circ}}{m_{DuT}\, g} \tag{5}$$

The CoG coordinate c can be directly derived from the torsional moment M_T since the lever is already perpendicular to the gravitational vector.

$$c = \frac{M_{T,0^\circ}}{m_{DuT}\, g} \tag{6}$$

To determine the third coordinate, the setup has to be rotated by 90° around a:

$$b = \frac{M_{T,90^\circ}}{m_{DuT}\, g} \tag{7}$$

The described measurement setup can be used in a first step to measure the body inertia relative to the S and R frame since these axes are known from the coordinate transformation. This case is trivial since normally, the body axes are not aligned to the coordinate frame axes (Figure 12).

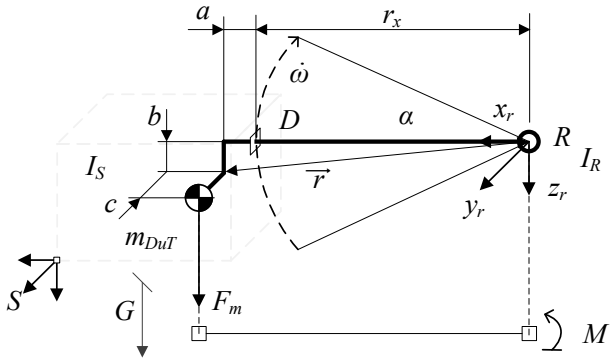

Figure 12. Reduced mechanical system, inertia determination.

Therefore, the body system has to be exposed to a constant angular acceleration while the resulting torque around the rotational axis is measured. For the derivation, the system is assumed to be two-dimensional, rotating around the *R* system's y axis. Using the Huygens–Steiner theorem and the resulting radius *r*, we find

$$I_{S,y} = I_{R,y} - m_{DuT} r^2 \tag{8}$$

and the function for the resulting rotational torque

$$\vec{M_1} = I_{R,y}\, \vec{\dot{\omega}} \tag{9}$$

The body inertia in the *S* frame is calculated as

$$I_{S,y} = \frac{M_1}{\dot{\omega}} - m_{DuT}\sqrt{(r_1 + a)^2 + b^2} \tag{10}$$

To determine the major axes θ of inertia of the body system, an iterative approach has to be used. Here, the body must rotate around the CoG for the *S* system coordinate axes while following an algorithm to minimize Equation (10) for each axis (Figure 13).

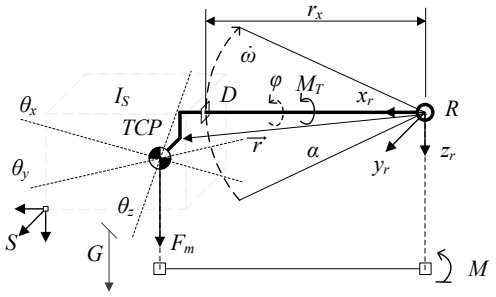

Figure 13. Reduced mechanical system and body axis determination.

2.3.2. Mass Determination Approach

The mass determination faces the principal problem that in the first setup, the CoG-position relative to the robot TCP coordinate frame is only known via engineering data, such as CAD analyses. To develop a robust algorithm for any mass determination problem to be solved, it is therefore assumed that the CoG coordinate transformation is generally unknown. The mechanical system that is defined by the robotic system and the device under test (DuT) is shown in Figure 14.

As can be seen, the mass of the DuT can be determined by its resulting torques. Since the respective levers from the TCP to the DuT CoG are, per definition, unknown, a relative measurement of the robot axis torques M_{A3} and M_{A5} is used. To reduce the measurement error, it has to be made sure that the gravity vector is aligned with the TCP axis perpendicular to the robot axes. The resulting torques are defined by the robot arm levers and the yet unknown CoG lever as per Equation (4):

$$m_{DuT} = \frac{M_{A3} - M_{A5}}{g\,(r_{A3} - r_{A5})} \tag{11}$$

Equation (11) shows the baseline algorithm of all consecutive measurements. Since, in a real application case, the DuT is not directly attached to the robot TCP, the additional mass fraction m_f has to be covered by the algorithm. Equation (11) has to be expanded to cover any type of mounting fixture that is attached to the robot hand mount to hold the DuT in place, as well as the torque balance resulting from the robot mechanics itself. The torque balance thus changes to

$$M_{A3} = M_{f,A3} + M_{DuT,A3} + M_{0,A3} \tag{12}$$

$$M_{A5} = M_{f,A5} + M_{DuT,A5} + M_{0,A5} \tag{13}$$

With the given forces and levers, this leads to

$$m_{DuT} = \frac{(M_{A3} - M_{0,A3}) - (M_{A5} - M_{0,A5})}{g\,(r_{A3} - r_{A5})} - m_f \tag{14}$$

Since the planetary gears, actuator axle friction and synchronous belts of the robot's drive have a significant impact on the measured gear torques at the output side, a calibration function $K = f(m,M)$ is introduced to cover systematic errors from the kinematic chain, leading to the defining equation of the robotic in-line mass determination:

$$m_{DuT} = \left(\frac{(K(M_{A3})M_{A3} - M_{0,A3}) - (K(M_{A5})M_{A5} - M_{0,A5})}{g\,(r_{A3} - r_{A5})}\right) - m_f \tag{15}$$

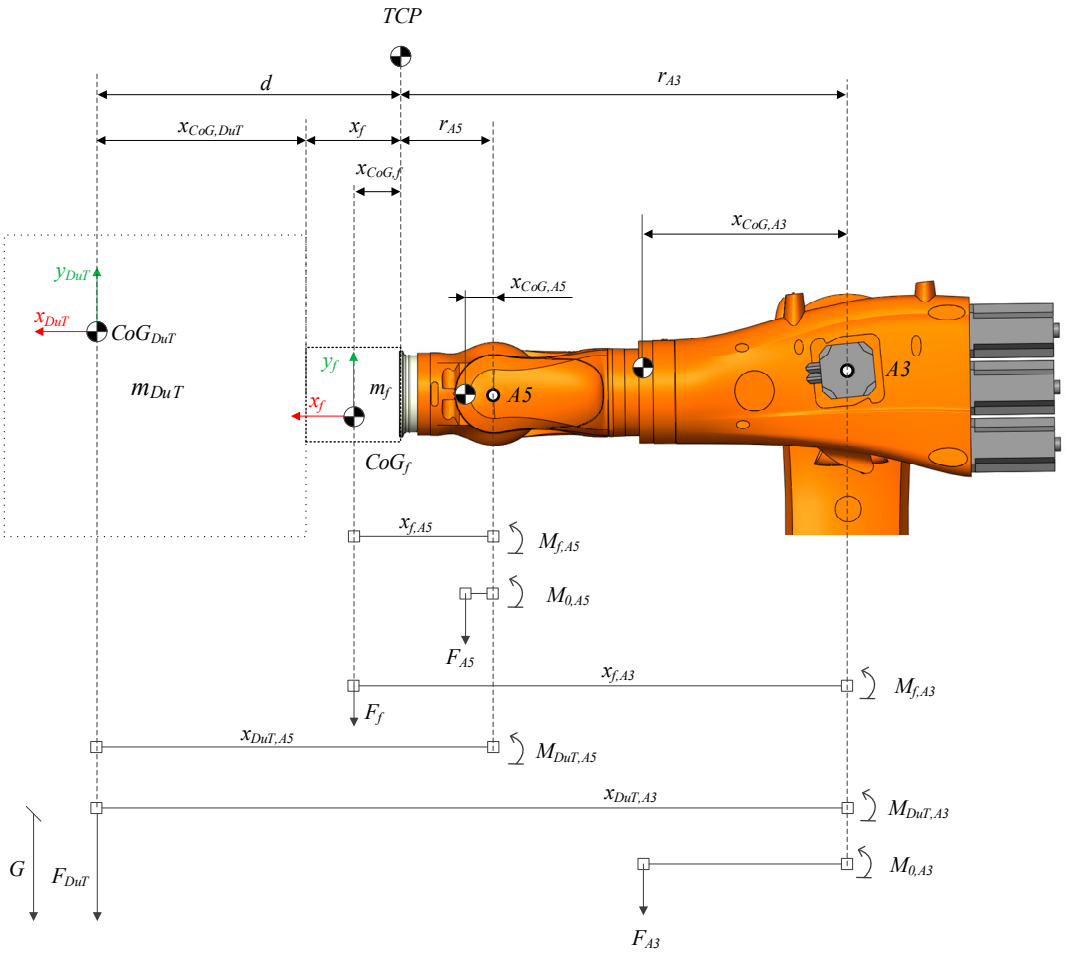

Figure 14. Mechanical system for DuT mass determination with mounting fixture f.

2.4. System Calibration

As shown before, a robust and repeatable torque measurement is the foundation of the robotic mass property determination. To achieve the necessary technological readiness, several options for torque calibration are examined and presented in the following section. Generally, it can be distinguished between mass based and torque-based calibration. The difference in the approaches lies in the necessity of knowledge of the calibration body CoG. The mass-based approach allows for a direct correlation between calibration mass and the DuT mass, while the torque-based approach allows a direct correlation between the resulting torque of the calibration body and the measured torque. The latter allows us to

extend the calibration towards CoG and inertia measurement, while the first option offers a quick and easy way to design a robust principle for torque measurement and to detect and eliminate possible obstacles. For both approaches, the same data acquisition methods will be applied, using the robot-inherent maintenance interface to extract both kinematic status and physical parameters during the calibration movement.

2.4.1. Data Acquisition

To keep financial expenditures low, only the robot controller telemetry data without any external sensor application are used for data acquisition. This method is, in the defined context, mandatory for the RGSE to be an economically advantageous approach. The robot telemetry data can be accessed via the controller maintenance interface. The controller software allows for the definition of the recording patterns for all controller parameters for a defined number of samples, depending on the sampling rate. Sampling differs depending on the nature of the telemetry parameters and cannot be modified. The pre-defined telemetry samples (hence called traces) can be actively called in the frame of any given Kuka Robot Language (KRL) script and are stored on the hand controller hard drive. The necessary data comprises the torque at the A3 gear output, the A5 gear output and the motor temperatures, as well as the motor current at both actuators. The given gear torques are pre-processed by the robot controller and are derived from the motor current since the robot has no built-in torque sensors. Therefore, the data quality of the measured torques is critical, making it necessary to perform a set of post-processing steps. The motor current and temperature are recorded for statistical analysis. It is assumed that the motor temperature will have some effect on the quality of the motor current data and therefore on the resulting torque, determined by the controller's post-processing algorithm, which is by default unknown to the user.

The tool mass settings are defined to −1 kg, enabling the "unknown payload mass" mode.

The number of samples and thus the number of measurements is limited by the reserved buffer size of the controller, making it necessary to cluster measurements to achieve a statistically valid number of samples (Figure 15). For the time being, the acquired data is extracted manually via a USB stick. A functional network solution for data extraction is still under development. The measurement time to obtain only the torque data for a full calibration is estimated to be 480 min, not counting the time for manual extraction and post-processing. All post-processing steps are carried out using MATLAB with the statistics toolbox.

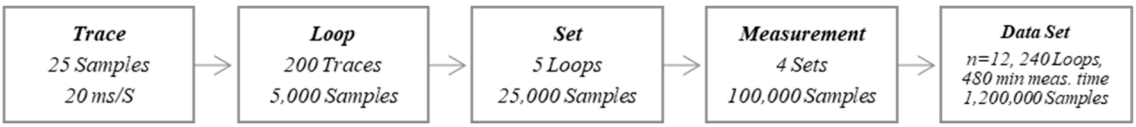

Figure 15. Measurement chain for calibration data acquisition.

2.4.2. Mass-Based Calibration

To determine the calibration curve of mass versus axis torque, a symmetric test setup is developed to gain a sufficient amount of data points within the robot's certified mass and torque envelope (M_{max} = 3.33 kN at $A5$, Figure 16). In order to carry out the required reference measurements, it is recommended to use calibration bodies whose weight and center of gravity are known. It is best to use geometrically simple calibration bodies such as cubes or plates to avoid unnecessary complexity. In addition, the weight intervals chosen must/should cover the robot's operating range as linearly as possible.

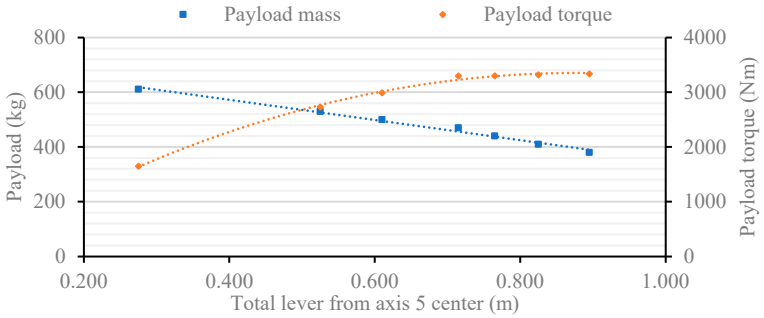

Figure 16. Integral load diagram for a KUKA KR500 R2830 for *maximum dynamic range*; maximum payload 611 kg and maximum torque 3.33 kN [7].

Note: The given values for the maximum torque are defined for the robot's maximum allowed movement dynamics of up to 120°/s *per axis*. Therefore, the possible static and low dynamic loads are much higher than the chosen ones. However, for safety reasons the examination focuses strictly on the defined load diagram without pushing the torque range over the limits for the initial approach.

The test assembly makes use of symmetrical steel calibration bodies of 20.9 kg each. For a first mass-based calibration approach, the calibration bodies are stacked to the multi-payload adapter of the robot's hand mount. The shift of the calibration DuTs CoG due to the increasing depth does not affect the measurement outcome since Equation 16 is applicable in this setup. The occurrence of disturbing torques around the axes is negligible because both calibration bodies and MPA are of axis symmetrical shape (Figure 17).

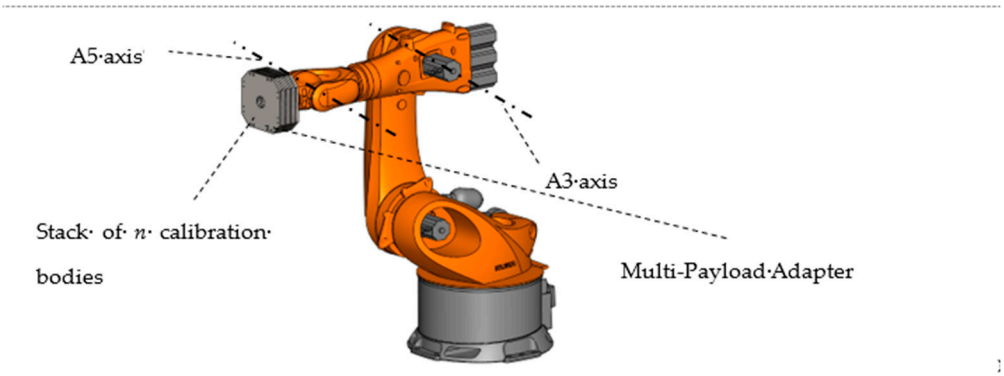

Figure 17. Mass-based calibration assembly: stack of 10 calibration bodies at the MPA.

To perform the calibration, 12 measurements are conducted in the given order. The resulting torques around axes *A*3 and *A*5, as well as the motor currents and motor temperatures at both axes, are recorded:

1. *1× without any weight at the hand flange;*
2. *1× with MPA for process validation;*
3. *10× with an increasing number of calibration bodies nCB.*

In a first iteration loop, the actual measurement algorithm is developed in a series of test runs. The resulting sample sets are then analyzed for drifting. The drifting characteristics are examined for correlations with the measured parameters of time, temperature and current using a set of MATLAB scripts.

Efforts are made to optimize the principle of data acquisition by technical means rather than statistical ones in order to minimize drift and reduce the effort required for n-dimensional calibration. After a sufficient optimum is reached, the actual calibration run is conducted to determine the calibration function *K*.

For the calibration, the test adapter torque is varied by the applied number of calibration bodies. For each of the 10 envisaged measurements, after an initial settle time

of 2 × 2 s, the motor current-induced torque at the drive of the $A5$ axis is recorded in a pattern according to Figure 14. The data are extracted and post-processed for each point using a double arithmetic average reflecting the data sampling method of j measurements comprising i samples:

$$M(n_{CB}, x_{CoG,CB}) = \frac{1}{m}\sum_{j=1}^{m}\left(\frac{1}{n}\sum_{i=1}^{n} M_i\right)_j \tag{16}$$

2.4.3. Torque-Based Calibration

To extend the possible maximum calibration torques relative to the mass-based calibration approach, the calibration bodies defined for the mass-based approach can be mounted on a test adapter comprising a construction profile guide rail (Figure 18). The guide rail is fixed to the robot's multi-payload-adapter at the hand mount. The maximum achievable lever length towards $A5$ is 1480 mm.

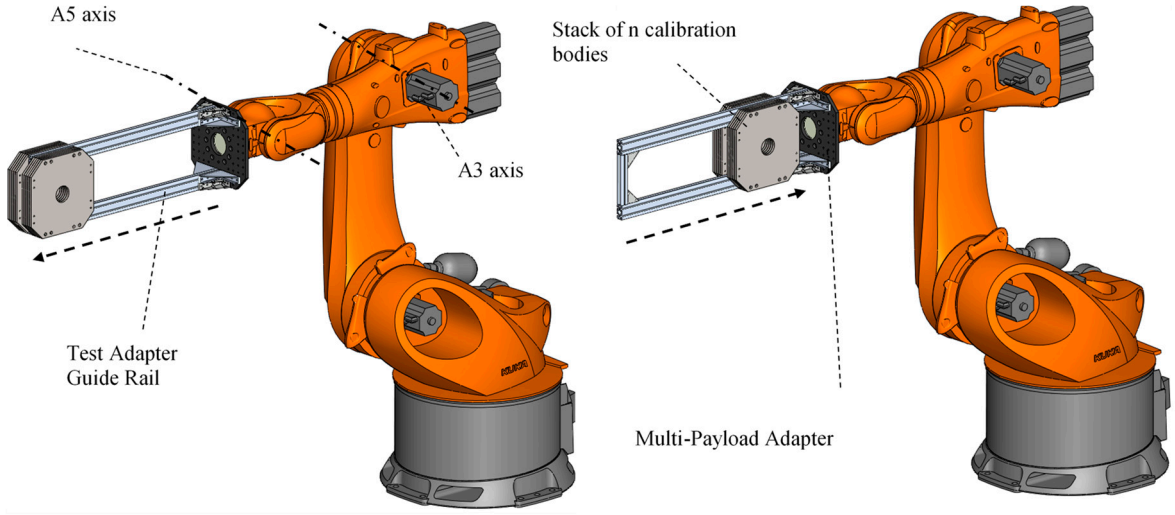

Figure 18. Torque-based calibration assembly: maximum lever (**left**) and minimum lever (**right**).

Since the calibration bodies are stackable, the total mass vary from 0 to 209 kg (with symmetrical mounting) in steps of 20.9 kg. This system allows for a torque range of 216 Nm (test adapter only) to 3245.5 Nm at the maximum lever with 10 calibration bodies at $A5$.

The calculation of the applied load has to take all acting torques at the center of the robot axis $A5$ into account. The mechanical system consists of the force-balanced hand pivot housing, which holds the $A5$ axis, the test adapter weight and the weight of the calibration bodies and their respective lever.

From the given forces, all but the calibration weights are static. Since the hand pivot housing is not perfectly balanced, resulting in an unknown residual torque $M_{0,A5}$, the total torque at axis $A5$ is

$$M_{A5} = \sum M_{i,5} = g(n_{CB} m_{CB} x_{CoG,CB,A5} + m_{TA} x_{CoG,TA,A5}) + M_{0,A5} \tag{17}$$

A similar approach is taken for axis $A3$, so the resulting torque is calculated as follows:

$$M_{A3} = \sum M_{i,3} = g(n_{CB} m_{CB} x_{CoG,CB,A3} + m_{TA} x_{CoG,TA,A3}) + M_{0,A3} \tag{18}$$

The residual torques at $A5$ and $A3$ are defined by the robot's body weight, the bearing and gear torques of the robot mechanics and the robot control algorithm post-processing. These torques cannot be analytically derived from the mechanical setup and have to be determined within the calibration process. The mass properties of the test adapter and calibration bodies are given in Table A1 in the Appendix A. The test adapter mass properties

allow for application of the nominal torque ranges shown in Figure 19 for calibration bodies only relative to the relative lever x_{CB} (Figure 20). The average mass error for each calibration body is measured to be <<1%.

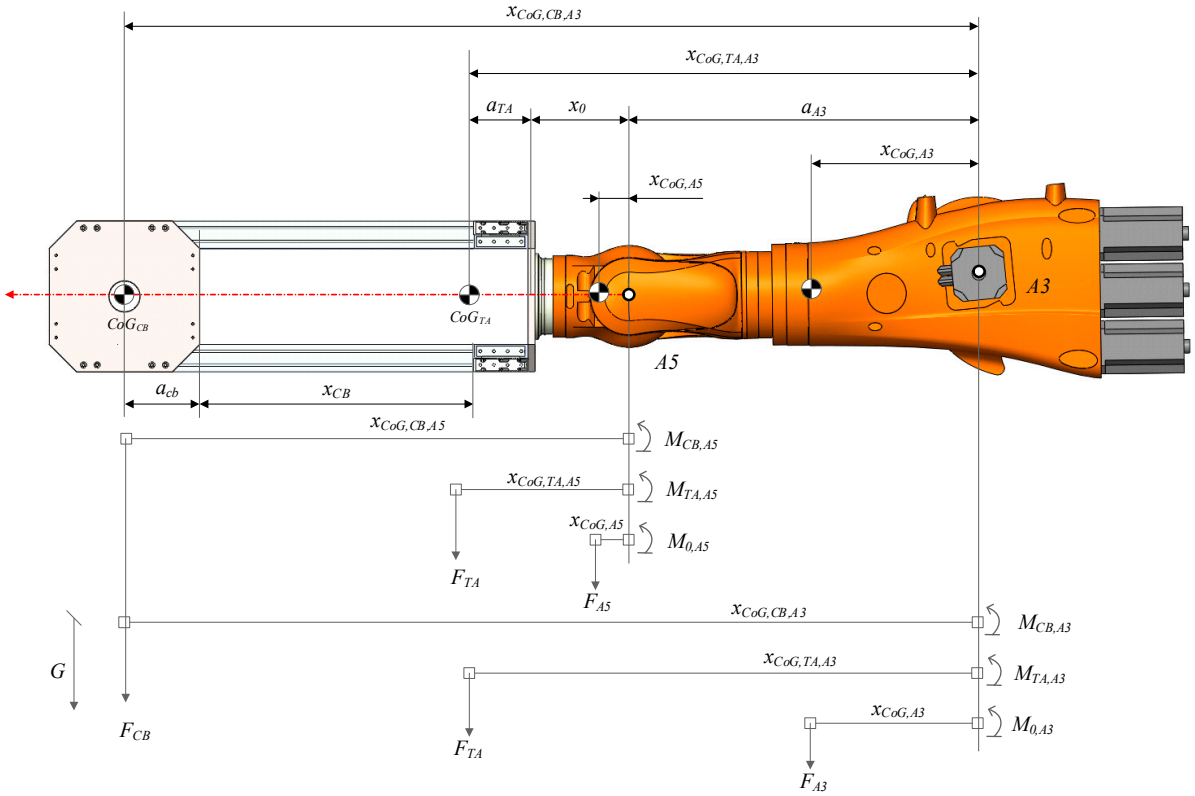

Figure 19. Torque-based calibration approach: geometry and loads along test setup for *A*3 and *A*5.

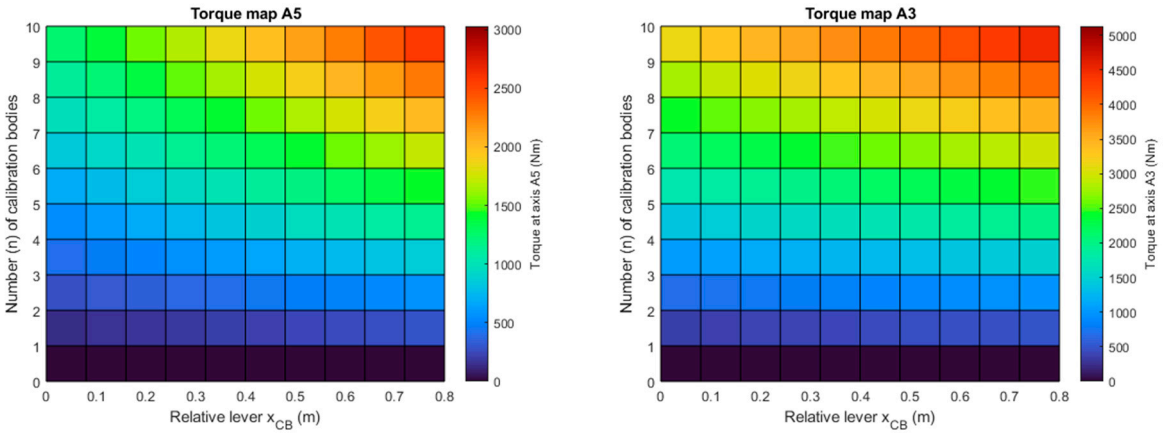

Figure 20. Achievable calibration torque at axis *A*5 and axis *A*3.

2.4.4. Torque Measurement Algorithm

To determine the most suitable measurement and post-processing algorithms, several explorative pre-tests were conducted. The findings, resulting methods, data acquisition and data processing are described in this section.

For all tests, the RGSE was moved to a horizontal position with $\varphi' = 55°$ as shown in Figure 21, while acquiring data with the algorithm described in Figure 16. This position has been chosen since it is very close to the robot's standard transport configuration, which is designed to provide maximum stability for craning and floor movement. Since the auto-break function of the robot has to be overridden by a small break release movement

every 20 s of measurement time, the transient behavior is repeatedly restarted at least every 20th trace. For the break release, the robot rotates both measurement axes by an equal angular distance ($\varphi' = 35°$) to actively counteract the effects of gear solicitation.

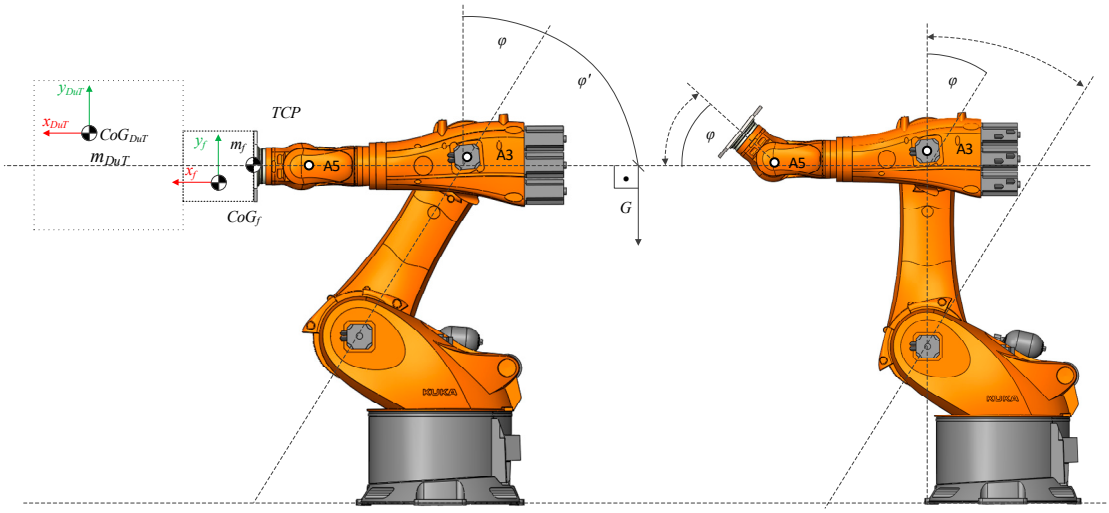

Figure 21. Mass determination measurement position (**left**) and break release movement (**right**).

During the tests, a drifting behavior was observed, which was repeated at the interval of the break release movement due to the motor temperature. As can be seen from the samples of the residual torque measurement, exemplarily given in Figure 22, the motor temperature causes the measured torque to converge towards an equilibrium state, increasing the standard deviation of each loop. This is assumed to be caused by the increase in the electrical resistivity in the motor due to heating over longer periods of operation time, requiring higher motor currents.

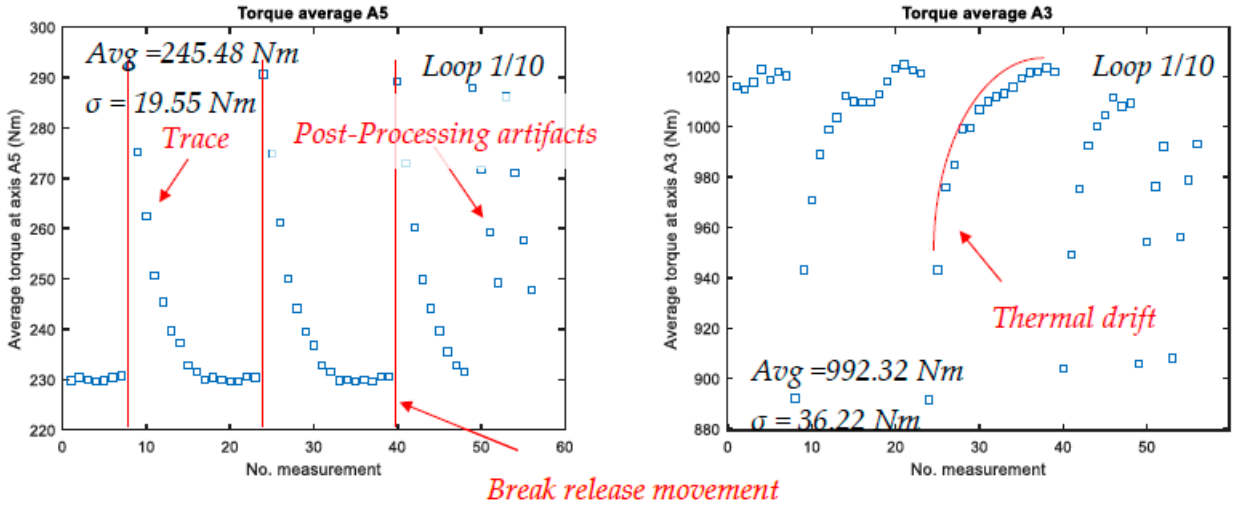

Figure 22. Resulting torque for axes A3 and A5, n = 0, loop 1/10.

It was found that the transient is trace-inherent and independent of the number of loops, which highlights the effect of the system temperature as the robot gradually heats up during the course of the calibration process.

Since the primary goal is a robust measurement of the axis torque, meaning a reduction in the observed standard deviation, two consecutive paths are followed:

A. Physical reduction in the observed standard deviation in the measurement sample.
B. Algorithmic reduction in the observed standard deviation.

For all traces, a mean temperature gradient of about 2 °C over the course of one trace was observed. Since the surrounding clean room is temperature controlled, it is assumed that the underlying heat transfer mechanism allows for constant cooling of the motor housing. Since the RGSE is primarily static, as opposed to the nominal industrial mode of operation, a cold start for the actuators is the nominal case. The measurement algorithm would have to be adapted to improve the temperature stability in the actuators, as the thermal transient seems to be a major source of measurement accuracy.

From an algorithmic perspective, there are two ways to reduce the standard deviation. The first and simplest way is to remove outliers using a cropping algorithm that cuts off all values that deviate from the mean by more than a predefined number of standard deviations. To enhance effectiveness, the cropping window can be reduced during pre-tests. Secondly, the data can be smoothed by statistical means, further reducing the standard deviation.

For the time being, a combination of all three principals for pre-processing is used:

A. A pre-heating motion ("warm-up move") to increase the overall temperature of the robot, reducing the temperature gradients between the motor and housing.
B. A cropping algorithm that first removes xσ outliers from the loops.
C. A filter algorithm to smooth the measurement data.

The algorithm for the torque calibration and torque measurement is then defined as follows (Figures 23 and 24):

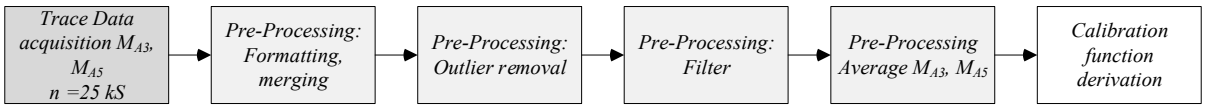

Figure 23. Data acquisition and processing loop for a system calibration.

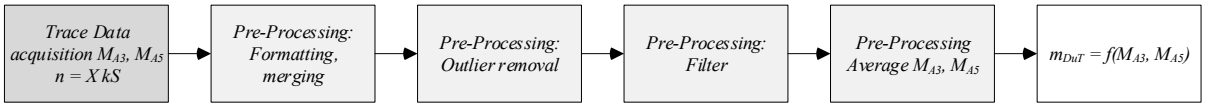

Figure 24. Data acquisition and processing loop for in-line mass determination.

To determine the calibration function $K(M_{A1})$ and $K(M_{A2})$ and to optimize the preprocessing parameters for outlier removal and cropping, a sensitivity analysis was performed on the raw calibration data.

2.4.5. Calibration Data Results

A total of 14 measurements were performed for calibration, 11 e in a mass- and three in a torque-based measurement setup. A total of 21 to 31kS of valid data points were collected for each calibration body configuration (Table 1). The measured 0-bias for $A3$ is 1320.46 Nm, and the 0-bias for $A5$ is 315.96 Nm. All calculations were carried out using normalized values.

As shown in Figure 25 both calibration curves deviate significantly from the expected behavior. Since the axis torque is directly derived from the motor current via the robot controller, a significant impact of the motor temperature on the measured values is to be expected, as can be seen in Figure 20. From the data, a thermal drift of 30.4% until equilibrium can be observed on A5, while the thermal drift on A3 is only 14.4%. Considering the cold-start conditions, it can be assumed that a certain part of the acting torque is compensated by gear friction and cold lubricant. The significantly higher thermal impact on A5 may now lead to an overestimation of the control algorithm, while the A3 torque remains under-predicted. This effect has to be analyzed further in future calibration runs.

Table 1. Expected and resulting torques for axes *A*3 and *A*5 with calculated deviation.

Calibration Type	n_{CB}	m (kg)	l_{A3} (m)	l_{A5} (m)	$M_{A3,norm}$ (Nm)	$M_{A5,norm}$ (Nm)	$M_{A3,norm,meas}$ (Nm)	σ_{MA3} (Nm)	$M_{A5,norm,meas}$ (Nm)	σ_{MA5} (Nm)	ΔM_{A3}	ΔM_{A5}
Mass	0 (MPA)	0.00	1.3100	0.2850	0.00	0.00	0.00	4.94	0.00	12.47	0.0000	0.0000
Mass	1	20.93	1.3275	0.3025	268.47	58.01	248.15	7.40	62.90	11.42	1.0819	0.9222
Mass	2	41.86	1.3350	0.3100	540.02	119.09	495.68	9.81	132.09	6.91	1.0895	0.9016
Mass	3	62.79	1.3425	0.3175	814.66	183.26	744.40	6.94	194.28	9.35	1.0944	0.9433
Mass	4	83.72	1.3500	0.3250	1092.37	250.51	1002.55	7.10	283.33	10.40	1.0896	0.8841
Mass	5	104.65	1.3575	0.3325	1373.16	320.83	1253.16	9.33	371.47	9.77	1.0958	0.8637
Mass	6	125.59	1.3650	0.3400	1657.03	394.24	1512.77	8.21	454.26	7.07	1.0954	0.8679
Mass	7	146.52	1.3725	0.3475	1943.98	470.72	1762.82	8.31	554.79	9.96	1.1028	0.8485
Mass	8	167.45	1.3800	0.3550	2234.02	550.29	2031.47	9.67	657.26	9.26	1.0997	0.8373
Mass	9	188.38	1.3875	0.3625	2527.13	632.94	2303.79	12.21	755.79	18.00	1.0969	0.8375
Mass	10	209.31	1.3950	0.3700	2823.32	718.66	2581.00	20.73	838.55	17.45	1.0939	0.8570
Torque	10	228.51	1.8200	0.7950	4068.67	1781.26	3612.08	14.03	1974.26	12.67	1.1264	0.9022
Torque	10	228.51	2.0700	1.0450	4582.00	2294.60	4069.84	23.87	2630.37	27.35	1.1258	0.8723
Torque	10	228.51	2.3200	1.2950	5095.33	2807.93	4505.90	19.55	3187.81	13.91	1.1308	0.8808

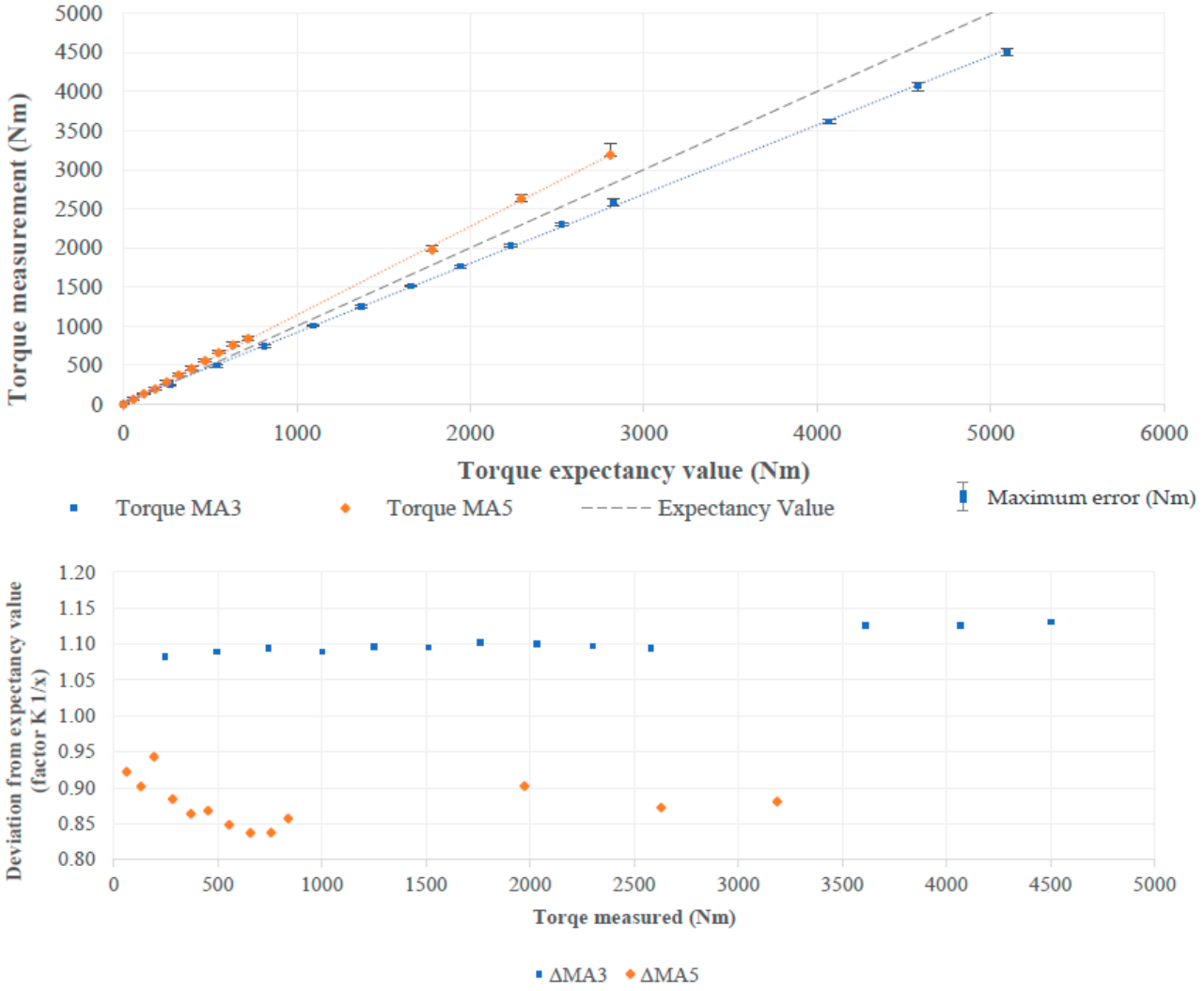

Figure 25. Torque calibration curves and calibration factor for axes *A*3, *A*5.

The overall distribution of the calibration measurements suggests that the calibration factor *K* can be described by a polynomial fit as a function of the measured torque for *A*3, while *A*5 is better interpolated by an exponential function. The definition and optimization of the *K*-function are described in the following sections.

2.4.6. Calibration Factor Fit and Optimization

To optimize the suggested mass determination algorithm, the acquired calibration data undergoes a parameter study loop (Figure 26). Calibration factor K is intended to correct for the torque delta between the expected value of the calibration body mass and the post-processed raw data, approximated by a second-order polynomial function. The loop will test the following interdependencies:

- The window in which outliers are removed (1, 2, 3σ);
- The filter algorithm (moving mean, Gauß, . . .);
- The filter algorithm characteristics;
- The pre-processing sequence: forward (filtering, cropping)/backward (cropping, filtering);
- The evaluation of the K-function parameters.

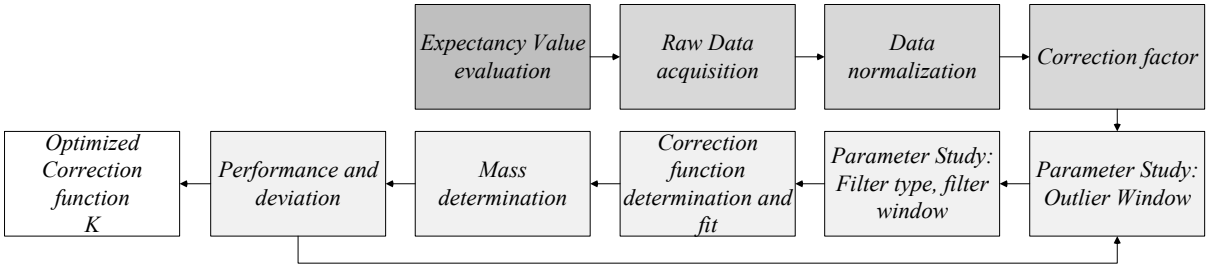

Figure 26. Parameter study flow chart.

The parameter study was performed in a two-step approach. First, exploratory tests were conducted using different combinations of optimization parameters to evaluate whether a preferred path can be identified. This part of the study revealed that the most promising results are obtained via a combination of a 1σ or 2σ outlier removal followed by a simple centered moving mean filter. This combination was further investigated by varying the filter window and the outlier removal boundaries. The calibration factor for axis 3 will be approximated by a polynomial fit (R^2 = 0.8922):

$$K_{A3}(M_{A3}) = a_1 M_{A3}^2 + a_2 M_{A3} + a_3 \tag{19}$$

The best fit for axis 5 is an exponential function (R^2 = 0.8076):

$$K_{A5}(M_{A5}) = b_1 e^{(b_2 M_{A5})} + b_3 e^{(b_4 M_{A5})} \tag{20}$$

In total, Figure 27 surveys were performed, and the results with an R^2 greater than 0.88 are shown in Table A2 in Appendix A. A hand-picked method, where the filter window is manually selected for each calibration data set, results in the lowest mass error. Since this is not feasible for later automated measurements, an automated algorithm is required. A backward pre-processing with a leading outlier removal in the 1σ range followed by a moving average filter with a window size of 150 is chosen.

With the acquired pre-processing algorithm, the fit parameters of the mass determination algorithm can be calculated as follows:

$$m_{DUT} = \frac{M_{A3,norm}\left(a_1 M_{A3}^2 + a_2 M_{A3} + a_3\right) - M_{A5,norm}\left(b_1 e^{(b_2 M_{A5})} + b_3 e^{(b_4 M_{A5})}\right)}{g(\Delta r)} - m_f \tag{21}$$

Using Equation (10) and the given fit parameters, the mass of the calibration bodies can be calculated using a mean error of 0.6986% and a standard deviation of ±1.79 kg. The last three measurements were taken to evaluate the performance of the torque-based calculation with a maximum weight of 228.51 kg on different levers. As can be seen, the calculated mass values for the last three measurements are evenly distributed around the expected value,

but with a rather large standard deviation of up to 2%. It is therefore assumed that the measurement principle will show less performance for high-torque applications (Figure 28).

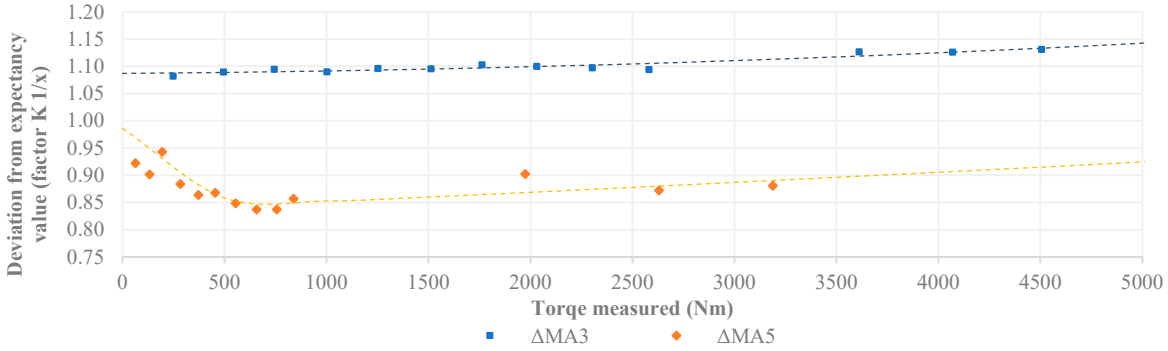

Figure 27. Polynomial fit function for *A*3, *A*5 correction factor.

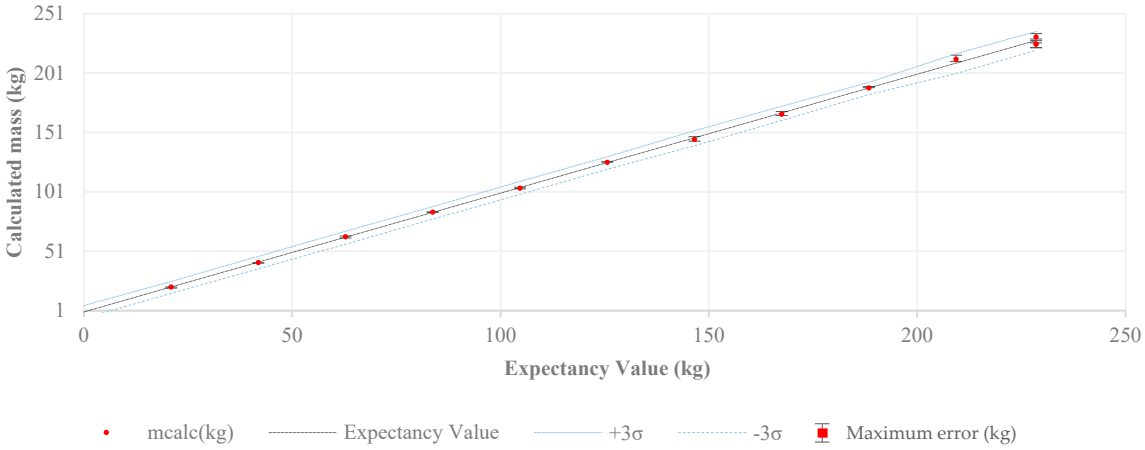

Figure 28. Calibration results and error corridor.

2.4.7. Algorithm Evaluation

A reference test was performed to validate the operability and robustness of the mass determination algorithms against asymmetrical payloads. For this test, the ReFEx (reusability flight experiment) wing box segment with its TCP-mounting structure was used. The test is designed in such a way that an in-line mass measurement during a spacecraft integration campaign is simulated and compared to a standard, crane-scale-based approach. The mass of the payload fixture is determined beforehand in a separate measurement (10.288 kg).

For the reference mass measurement, the payload is attached to the RGSE via its fixture on the MPA (Figure 29). The payload is placed in a detachment position while the crane scale and rigging are prepared. After preparation, the payload is fixed to the lifting jig and detached from the fixture by opening the payload clamp band. The RGSE is then retracted, and the free-hanging mass measurement is performed using a Kern HFB 300K100 crane scale. After measurement, the payload is re-attached to the RGSE by closing and securing the payload clamp band. The total time of the operation is measured, accumulating to 43 min. No PA processes have been performed during this operation. The dry mass of the payload is 107.3 $\pm$ 0.1 kg. Including the payload fixture, the total weight adds up to 117.6 $\pm$ 0.1 kg.

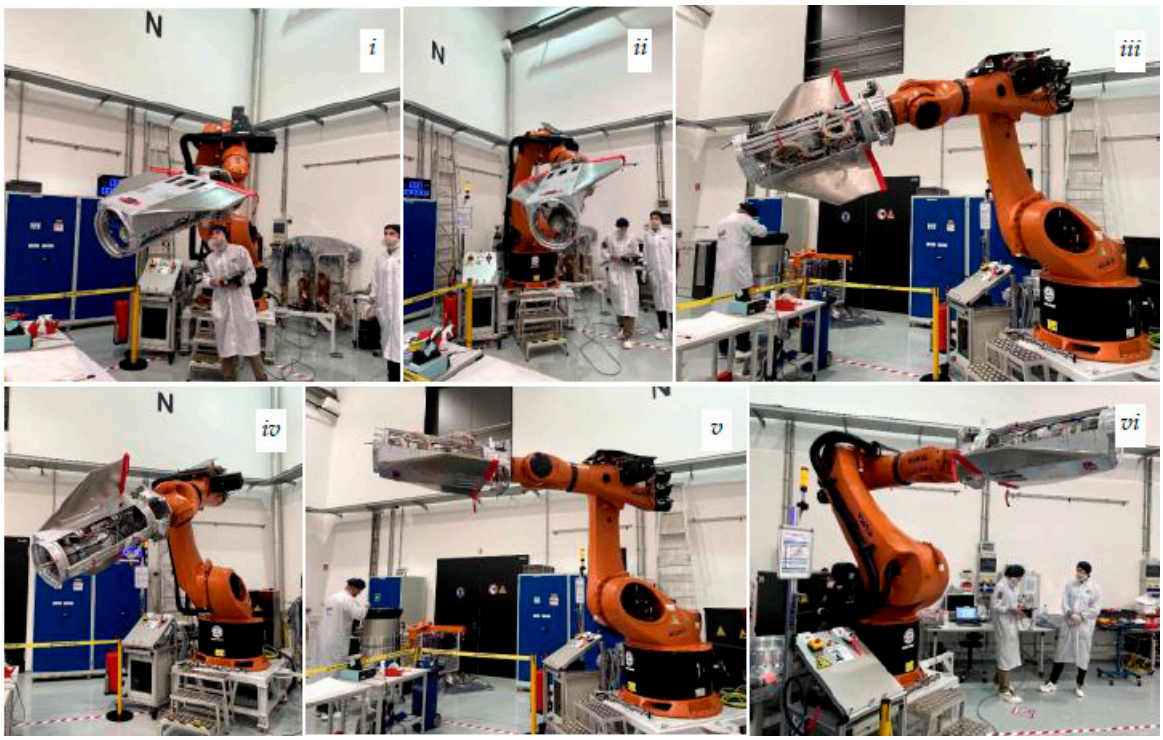

Figure 29. Validation payload mass determination. (***i–iv***): movement from operational to measurement position, (*v*): break release movement, (*vi*): measurement position.

For the in-line mass determination, the payload is also attached to the RGSE with a fixture and clamp band. The system starts in an operational position when the mass determination script is started. A total of 10 measurements accumulating a total of 10 kS were conducted to achieve statistical validity. The measurement runs, as well as data retrieval from the hand controller, were performed manually without further automation. The payload is brought to the measurement position and performs nine break release movements in between the measurement runs. Including manual data retrieval, the total time for each 1 kS measurement run accumulates to 2:30 min, adding up to a total measurement time of 25 min from beginning to end. No PA operations were conducted either. The pre-processing algorithm reduces the initially acquired 10 kS to a total of 4253 kS of valid data points, resulting in a total determined mass of 117.94 ± 0.707 kg. The relevant parameters are summarized in Table 2.

Table 2. Reference measurement results.

Parameter	Reference Measurement	In-Line Mass Determination
Total time of operation (min)	43	25
Total number of operators	3	1
PA processes	0	0
Total working hours (min)	129	25
Spanning activities	2	0
Payload fixture mass (kg)	10.288	
Total measured mass (kg)	107.3 ± 0.1	117.94 ± 0.7
Net mass (kg)	107.3 ± 0.1	107.65 ± 0.7

3. Results and Discussion

We demonstrated that robot-based ground support equipment can effectively be used during small- and medium-sized spacecraft integration and that it is possible to implement an in-line mass determination algorithm without external sensory interfaces only by using the telemetry data provided by the robot. The setup was successfully used

during the integration of the MMX rover structural and flight models as an integration aid in a collaborative setup with the operators and product assurance. Particle contamination and ESD problems could be ruled out by continuous accompanying measurements.

Additionally, it has been shown that the six DoF capabilities of the MGSE setup significantly improved operator ergonomics [10] and can be used to aid precise IMU alignment [11] by making use of the robot's re-positioning capabilities.

Nevertheless, since the usage of the robotic GSE was not envisaged during the MMX rover development, the design of the DuT fixture was improvised, making use of the static, standard GSE foreseen to be used for integration. For future missions, the adaptability to the robotic GSE has to be implemented in the top-level requirements to minimize the impact on the in-line GSE development during phase C/D.

For mass determination, a calibration function with sufficient precision using a suitable data pre-processing algorithm could be derived from an extensive calibration campaign. After sufficient calibration, the described mass determination algorithm is able to perform a prediction in the range of 0–228 kg with an average error of 0.6986%.

For a reference measurement, an asymmetrical spacecraft body with a calibrated mass of 107.3 $\pm$ 0.1 kg was used.

Using a dedicated software tool, a measurement with a total of 10 kS was performed without alteration in the DuT configuration in a total time of 25 min over the robot's manual programming and control interface in a semi-automated process. Using the above-described determination algorithm, the test resulted in a total determined mass of 117.93 $\pm$ 0.7 kg (1σ). In contrast, the same measurement using a crane-scale setup took a total of 43 min, including two re-spanning operations, not considering the time needed to prepare the necessary handling procedures.

From ECSS-E-10-03C [5], a maximum error of $\pm$0.05% is envisaged for mass measurements, as well as a CoG offset of 2.5 mm long and 1 mm perpendicular to the launch axis. For MoI, a total error of $\pm$3% is allowed. The given mass measurement with the non-optimized algorithm is thus one order of magnitude off the ECSS requirement, but the same applies to any off-the-shelf crane scale. It can safely be assumed that this impacts the CoG and MoI measurements in the same manner.

As can be seen from the acquired data (Table 2), the in-line mass determination differs significantly from the classical approach. While the total precision of the mass measurement is lower, with the measurement error still in the same order of magnitude as the reference measurement, the total operational effort is reduced significantly by a factor of approximately 5 compared to the reference test in terms of total working hours. Furthermore, the overall risk generated by the re-spanning and craning operations is reduced to zero, resulting in a further reduction of PA effort.

The overall effort to achieve a stable prediction method is rather high. For the given setup, a sufficient calibration device must be procured and applied, leading to an individual calibration function of each robotic system. Nevertheless, this is anticipated in the first place, since one goal of the investigation was to show the possibility of operating such a system off the shelf without further external hardware or software solutions. In the ongoing investigation, comparing the calibration effort to procure streamlined software solutions provided by system manufacturers to obtain a better view of the RoI will be considered. An auto-calibration device is currently under development to speed up the process.

Long-term calibration stability is a point that has yet to be determined since the method has just been recently rolled out. Considering the operational approach for the GSE and all involved safety aspects, the overall operational time of the mechanical system approaches nearly zero compared to the actual design case. The robot is positioned in a defined integration position with active breaks and de-activated actuators basically all the time while re-positioning activities seldom happen between procedural activities. Therefore, it is safe to assume that wear effects in the mechanical system will not have an impact on the measurements in a relevant time frame. Only the lubrication quality should be checked regularly, and aged lubricant should be replaced, but this is part of the nominal

maintenance scheme. The impact of the lubricant quality on the measurement has yet to be determined.

This shows that even a partly automated approach provides a significant advantage in operation time and risk reduction over the classical operation. Nevertheless, for the operational mass determination, there is a need to automatize the process to make it practically usable. The robot is necessarily operated in an unconfined configuration without caging in a COBOT manner to allow for direct interaction between robot and operator. To guarantee the safety of all operators, the system is technically blocked from being operated outside of the robot's manual programming mode, which allows for a maximum cartesian movement speed of 200 mm/s and disables all autonomous movement. By now, all calibration and measurement runs are carried out by hand, which takes a lot of time and effort for both calibration and data retrieval. For further development, it is foreseen to implement an automated interaction between the robot and software toolscape using the programmable controller interface and a network connection to the measurement computer (Figure 30). A sufficient safety concept for the verification runs has yet to be developed (Figure 31).

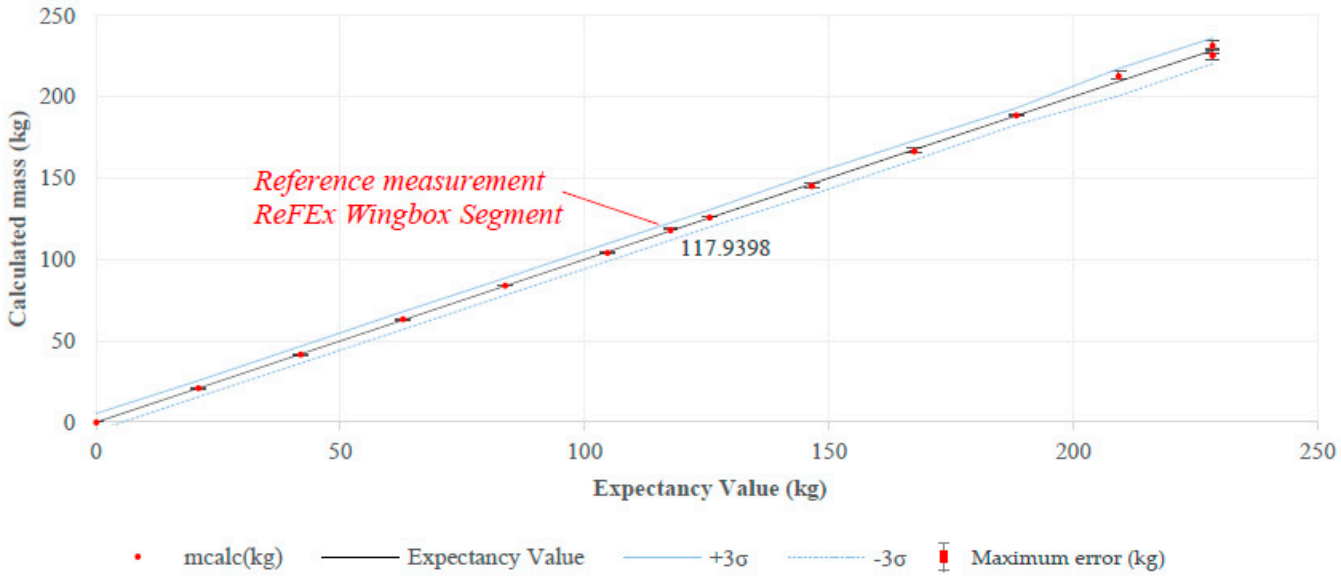

Figure 30. Reference measurement results for the ReFEx Wing box segment.

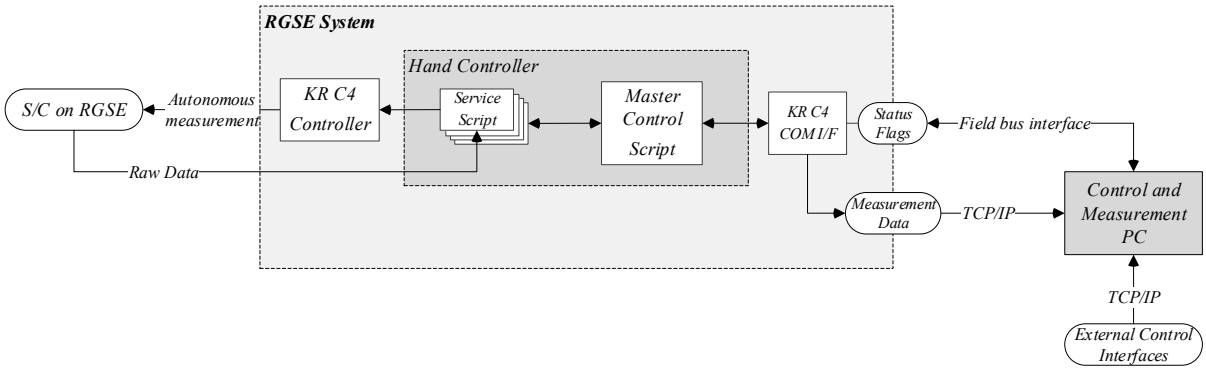

Figure 31. Automation principle of the in-line mass determination process.

The definition of the calibration algorithm has been conducted in such a way that sufficient speed to the overall RGSE development is added, yet this is not well optimized. By using a combination of explorational tests with a manual parameter study (such as outlier window, filter window and order of operation), the significance is rather limited.

This is increased by the limitations in total torque by the calibration test setup. For further improvements, a broad, automated optimization approach should be implemented to re-iterate the calibration function definition, especially the data pre-processing loop. For a quick optimization of the measurement results, a second tuning factor $k(m)$ could be implemented in Equation (22) for residual deviation. In contrast, the mechanical concept for the mass determination has already matured quite well, since the measurement position shown in Figure 19 significantly reduces the settling time of the setup after the imperative break release movement.

To determine the CoG position with sufficient accuracy, it is necessary to perform a similar calibration on one of the torsional axes ($A6$ or $A4$), yet it cannot be said at this point if the SNR of the torque measurement on the torsional axes is suited to estimate small CoG offsets. This has to be elaborated in a broad calibration campaign. To foster this effort, an automated calibration device based on the setup shown in Figure 17 to accelerate the evaluation process is currently under development. For inertia determination, it is vital, that the CoG position can be determined with optimized accuracy. The algorithm to derive the main axis rotation from a defined acceleration movement is currently under development. With this test setup, the resilience against vibration has yet to be shown. The whole process of CoG and inertia determination for spacecraft is an ongoing development and will be shown in consecutive follow-up publications.

4. Conclusions

In this article, a robotic GSE system setup is presented, and its operational prospects for usage and in-line verification have been elaborated and demonstrated. It has been shown that a robotic GSE has operational advantages over standard GSE solutions for the defined field.

An example was given to illustrate the opportunities and challenges of in-line mass determination. The necessary methods were developed and tested. It has been shown that the precise measurement of spacecraft mass without additional hardware is possible by using the existing technology of the robot. The subsequent work will be expanded by determining the center of gravity and the moments of inertia of the robot payload.

Even if the capability of performing in-line measurements with sufficient accuracy and the supportive capabilities towards operator ergonomics could be shown, there are still many challenges to overcome.

Since the mass determination algorithm is not fully optimized, the next step will be to design and operate an automatized calibration system to reduce the overall calibration effort and to automatically optimize the K-functions for all involved robot axes (A3–A6) without the need for further operator control. This will also pave the way for CoG and inertia determination. In parallel, the inertia determination algorithm is developed and tested as a mathematical model prior to being rolled out on the robotic system for demonstration.

To allow for a collaboration between robots and the PDM system for future augmented reality applications to further optimize the operator's workspace and ergonomics, a sufficient automation and safety concept has yet to be developed and demonstrated. This is carried out on a subscale RGSE development bench using a Kuka KR10-1440 as a demonstrator for software maturation in a dedicated laboratory.

Author Contributions: Conceptualization, S.K. (Sebastian Kottmeier) and B.S.; methodology, S.K. (Sebastian Kottmeier); software, P.W. and J.-L.K.; validation, S.K. (Sebastian Kottmeier) and P.W.; formal analysis, S.K. (Sebastian Kottmeier); investigation, P.W., S.K. (Sebastian Kottmeier) and J.-L.K.; resources, S.K. (Sebastian Kottmeier) and B.S.; data curation, S.K. (Sebastian Kottmeier); writing—original draft preparation, S.K. (Sebastian Kottmeier) and P.W.; writing—review and editing, T.-M.H., B.S., O.E. and S.K. (Sabine Klinkner); visualization, S.K. (Sebastian Kottmeier); supervision, S.K. (Sabine Klinkner) and T.-M.H.; project administration, B.S. and O.E.; funding acquisition, B.S. All authors have read and agreed to the published version of the manuscript.

Funding: The work was partly funded by the BMWK under contract number FKZ 68GX21003.

Data Availability Statement: The data used to support the findings of this study are included within the article.

Acknowledgments: Marco Scharringhausen (DLR) for developing the robot's IT interface and providing methodological support. The DLR MMX AIV Team for being the ergonomics study guinea pigs. The DLR Eu:CROPIS project for providing DuTs and equipment.

Conflicts of Interest: The authors declare no conflicts of interest.

Abbreviations and Acronyms

A		Axis
AIV		Assembly, Integration and Verification
AOCS		Attitude and Orbit Control System
Avg		Average
CAD		Computer-Aided Design
CB		Calibration Body
CoG		Centre of Gravity
D		Interface Position
DLR		Deutsches Zentrum für Luft- und Raumfahrt, German Aerospace Center
DuT		Device under Test
Eu:CROPIS		Euglena Combined Regenerative Organic Food Production In Space
f		Fixture
G		Gravitational force vector
GSE		Ground Support Equipment
K		Calibration function
KRL		Kuka Robot Language
kS		Kilo sample
m		Mass
MCI		Mass, Center of Gravity, Inertia
MGSE		Mechanical Ground Support Equipment
MMX		Martian Moons Exploration mission
MPA		Multi-Payload Adapter
PA		Product Assurance
PDM		Product Data Management
RGSE		Robotic Ground Support Equipment
SNR		Signal-to-Noise ratio
T1		Test Mode 1
TA		Test Adapter
TCP		Tool Center Point
norm		Normalized
meas		Measured
S/C		Spacecraft
DoF		Degree of Freedom
f		Mounting Fixture on MPA
CB		Calibration Body
ReFEx		Reusability Flight Experiment
RoI		Return of Investment
$\dot{\omega}$	$degs^{-2}$	Angular acceleration
a,*b*,*c*	-	CoG coordinate frame axes/lever
d	m	Distance
F	N	Force
g	ms^{-2}	Gravitational acceleration
I	kgm^2	Inertia
M	Nm	Linear Torque
m	kg	Mass
M_T	Nm	Torsional moment
n	-	Number of calibration bodies
r	m	Radius

R	-	Robot Coordinate Frame
S	-	Spacecraft Coordinate Frame
x	m	CoG lever distance
x,y,z	-	General coordinate frame axis vectors
x_0	m	Distance from A5 center point to hand mount interface
α	°	Angle of movement
$\theta_{a,b,c}$	-	Body axis vector
φ	°	Axis rotation
σ	-	Standard Deviation
r	M	Radius
G	ms^{-2}	Gravity Vector
$\varnothing$	mm	Diameter

Appendix A

Table A1. Mass properties of the torque-based test setup.

Parameter		Value	Unit
Mass of calibration body	m_{CB}	20.930	kg
Maximum number of calibration bodies	n_{CB}	10	--
Minimum lever of Calibration Body to $A5$	$x_{CoG,CB,A5,min}$	673	mm
Maximum lever of Calibration Body to $A5$	$x_{CoG,CB,A5,max}$	1475	mm
Minimum lever of Calibration Body to $A3$	$x_{CoG,CB,A3,min}$	1697	mm
Maximum lever of Calibration Body to $A3$	$x_{CoG,CB,A3,max}$	2499	mm
Torque of Test Adapter at $A5$	$M_{TA,A5}$	217.95	Nm
Torque of Test Adapter at $A3$	$M_{TA,A3}$	646.79	Nm

Table A2. Parameter study results. The selected method is in bold.

ID	Axis	Name	Sequence	Cropping Threshold	Filter	Window	R^2	M. Err. Axis (%)	M. Err. Mass (%)
A	A5	Moving average 1/500	PP backward	1 σ	Moving average	100	0.8992	−0.0585	0.9596
A	A3	Moving average 1/500	PP backward	1 σ	Moving average	100	0.9914	−0.1258	
B	A5	Moving average 1/1000	PP backward	1 σ	Moving average	50	0.8992	−0.1973	0.9593
B	A3	Moving average 1/1000	PP backward	1 σ	Moving average	50	0.9914	−0.1308	
C	A3	Moving average 1/10	PP forward	2 σ	Moving average	5000	0.9906	−0.4233	1.0389
C	A5	Moving average 1/10	PP forward	2 σ	Moving average	5000	0.895	−0.1318	
D	A5	Hand Pick	PP backward	1 σ	Moving average	200 ± 50	0.8883	−0.3271	0.6481
D	A3	Hand Pick	PP backward	1 σ	Moving average	200 ± 50	0.9907	−0.1275	
E	A3	Moving average 1/10	PP backward	2 σ	Moving average	5000	0.991	−0.123	0.979
E	A5	Moving average 1/10	PP backward	2 σ	Moving average	5000	0.8894	−0.6387	
F	***A5***	***Moving average 1/340***	***PP backward***	***1*** σ	***Moving average***	***150***	***0.8076***	***−0.3505***	***0.6986***
F	***A3***	***Moving average 1/340***	***PP backward***	***1*** σ	***Moving average***	***150***	***0.8922***	***−0.1022***	

Table A2. *Cont.*

ID	Axis	Name	Sequence	Cropping Threshold	Filter	Window	R^2	M. Err. Axis (%)	M. Err. Mass (%)
G	A3	Moving average 1/100	PP backward	2 σ	Moving average	500	0.991	−0.1736	1.0201
G	A5	Moving average 1/100	PP backward	2 σ	Moving average	500	0.8926	−0.3444	
H	A3	Moving average 1/100	PP forward	2 σ	Moving average	500	0.9906	−0.5654	1.0522
H	A5	Moving average 1/100	PP forward	2 σ	Moving average	5001	0.8952	−0.3939	
I	A5	Moving average 1/10	PP backward	1 σ	Moving average	5000	0.8791	−0.0383	0.8992
I	A3	Moving average 1/10	PP backward	1 σ	Moving average	5000	0.9916	−0.0873	
J	A5	Moving average 1/10	PP forward	1 σ	Moving average	5000	0.895	−0.1876	1.262
J	A3	Moving average 1/10	PP forward	1 σ	Moving average	5000	0.9906	1.3578	
K	A3	Moving average 1/100	PP backward	1 σ	Moving average	500	0.9907	−0.2825	1.0365
K	A5	Moving average 1/100	PP backward	1 σ	Moving average	500	0.8813	−0.2657	
L	A5	Moving average 1/100	PP forward	1 σ	Moving average	500	0.8942	−0.3774	1.0318
L	A3	Moving average 1/100	PP forward	1 σ	Moving average	500	0.9907	−0.1323	

Table A3. Calibration data of the chosen algorithm.

m (kg)	$M_{A3,norm,measured}$ (Nm)	$M_{A5,norm,measured}$ (Nm)	$M_{A3,calc}$ (Nm)	Error M_{A3} (%)	$M_{A5,calc}$ (Nm)	Error M_{A5} (%)	m_{calc} (kg)	Δm_{calc} (kg)	Δm_{calc} (%)
0.00	0.00	0.00	0.0000	0.0000	0.0000	0.0000	0.0000	0.0000	0.0000
20.93	248.15	62.90	269.9435	8.0728	59.7334	−5.3055	20.9055	−0.0254	0.1214
41.86	495.68	132.09	539.7103	8.1586	121.5279	−8.6918	41.5885	−0.2734	0.6531
62.79	744.40	194.28	811.4432	8.2617	174.9624	−11.0432	63.2984	0.5056	0.8051
83.72	1002.55	283.33	1094.3210	8.3865	249.6425	−13.4955	84.0037	0.2800	0.3344
104.65	1253.16	371.47	1369.9486	8.5249	322.6899	−15.1166	104.1504	−0.5042	0.4818
125.59	1512.77	454.26	1656.6694	8.6860	391.2194	−16.1135	125.8497	0.2641	0.2103
146.52	1762.82	554.79	1934.1480	8.8579	474.7966	−16.8481	145.1333	−1.3832	0.9441
167.45	2031.47	657.26	2233.8781	9.0609	560.6252	−17.2363	166.4059	−1.0415	0.6220
188.38	2303.79	755.79	2539.6143	9.2856	643.8402	−17.3876	188.5357	0.1574	0.0835
209.31	2581.00	838.55	2852.9990	9.5337	714.2412	−17.4043	212.7006	3.3913	1.6202
228.51	3612.08	1974.26	4041.3574	10.6221	1714.5695	−15.1459	231.4003	2.8921	1.2656
228.51	4069.84	2630.37	4582.3955	11.1852	2315.5348	−13.5967	225.4405	−3.0677	1.3425
228.51	4505.90	3187.81	5106.7059	11.7650	2838.7885	−12.2948	225.5456	−2.9626	1.2965
								Avg. Error:	***0.6986***

References

1. Delovski, T.; Düvel, C.; Greif, F.; Heidecker, A.; Kottmeier, S.; Mierheim, O.; Nohka, F.; Orlowski-Feldhusen, F. Eu:CROPIS AIV Program: Challenges and Solutions for a Spin-Stabilized Satellite Containing Biology. *Int. J. Aerosp. Eng.* **2019**, *2019*, 1–20. [CrossRef]
2. 'Basic MGSE Design'. Available online: https://www.esa.int/ESA_Multimedia/Images/2021/05/Installing_Juice_at_ESTEC6 (accessed on 20 February 2024).
3. Kottmeier, S.; Nohka, F.; Heidecker, A. Satelliten-Handhabungseinrichtung, Verwendung einer Satelliten-Handhabungseinrichtung und Satelliten-Baugruppe. Patent DE102017108847.4, 13 October 2016.
4. Suhr, B.; Benkel, M.; Brauer, U.; Corleis, U.; Ernst, H.; Esser, D.; Fischer, L.; Graf, A.; Hüffer, H.; Ho, T.M.; et al. Digital Collaborative Services and Tools for the Aeronautics and Space Sector. In Proceedings of the International Astronautical Congress, Paris, France, 18–22 September 2022.

5. ECSS Technical Authority—ECSS-E-10-03C Space Engineering–Testing, ESA ESTEC. Available online: https://ecss.nl/standard/ecss-e-st-10-03c-rev-1-testing-31-may-2022/ (accessed on 20 February 2024).
6. Michel, P.; Ulamec, S.; Böttger, U.; Grott, M.; Murdoch, N.; Vernazza, P.; Sunday, C.; Zhang, Y.; Valette, R.; Castellani, R.; et al. The MMX rover: Performing ins situ surface investigations on Phobos. *Earth Planets Space* **2022**, *74*. [CrossRef]
7. Rickmers, P.; Bauer, W.; Delovski, T.; Wübbels, G.; Kottmeier, S.; Klinkner, S. The Reusability Flight Experiment—ReFEx: Agile AIV Processes for Prototype Flight Experiments. In Proceedings of the International Astronautical Congress, Paris, France, 18–22 September 2022.
8. KR500 FORTEC Data Sheet'. Available online: https://www.kuka.com/-/media/kuka-down-loads/imported/8350ff3ca11642998dbdc81dcc2ed44c/0000233238_de.pdf?rev=bf55b64f81684c078c02ac014d72cd16&hash=10D71651A30CB6248FC43AF37FEB20A3 (accessed on 29 October 2023).
9. Rickmers, P.; Dumont, E.; Krummen, S.; Redondo Gutierrez, J.; Bussler, L.; Kottmeier, S.; Wübbels, G.; Martens, H.; Woicke, S.; Sagliano, M.; et al. The CALLISTO and ReFEx Flight Experiments at DLR—Challenges and Opportunities of a Wholistic Approach. In Proceedings of the ASCENSION Conference, Dresden, Germany, 9–13 September 2023.
10. Raupach, T. Evaluation of Augmented Reality and Robot-Assistance in Spacecraft AIV. Master's Thesis, University of Bremen, Bremen, Germany, 2023. Available online: https://elib.dlr.de/195025/ (accessed on 20 February 2024).
11. Gümpel, F. Evaluation of Robot-Assisted Spacecraft Alignment. Master's Thesis, University of Bremen, Bremen, Germany, 2023. Available online: https://elib.dlr.de/196013/ (accessed on 20 February 2024).